TU Delft

Optimal Lateral Escape Maneuvers for Microburst Encounters During Final Approach

H.G. Visser

Abstract

This report is concerned with the control and optimization of lateral escape trajectories in a microburst wind field for an aircraft on final approach. The performance index being minimized is the peak value of altitude drop. An extensive numerical effort has been undertaken to investigate the characteristics of open-loop extremal solutions for different locations of the microburst. If a sufficiently large bank angle limit is specified and the center of the microburst is not too far offset from the centerline extension of the approach runway, typically three trajectories can be found that satisfy the first-order necessary conditions of optimality, namely one trajectory that passes the microburst center to the left, one trajectory passing the center to the right and one trajectory passing right through the center. The results bear out that trajectories that feature lateral maneuvering to turn the aircraft away from the microburst center, generally offer a significant improvement in the escape capability of the aircraft in comparison to a trajectory that passes through the center. In contrast to non-turning escape maneuvers, lateral escape maneuvers often exhibit an initial climb, rather than a descent. It is conjectured that this behavior is a result of optimal energy management. A positional advantage within the flow field can be obtained by directing the flight away from the microburst center. On the other hand, the specific energy bleed-off rate should be kept as modest as possible. The optimization process establishes the optimal compromise between those two conflicting requirements. In addition to examining open-loop extremals, this report also describes the initial efforts to develop a closed-loop (feedback) guidance scheme that closely approximates the open-loop trajectories, but requires a relatively modest amount of information.

Table of Contents

Nomenclature

C_D, C_L	-	Aerodynamic coefficients
D	-	Drag force
E	-	Specific energy
g	-	Acceleration of gravity
H	-	Hamiltonian
h	-	Altitude
J	-	Performance index
K	-	Feedback gain
L	-	Lift force
r	-	Radial distance to microburst center
S	-	Wing area
T	-	Thrust
t	-	Time
V	-	Airspeed
W	-	Aircraft gross weight
W_h	-	Vertical windspeed
W_r	-	Radial (horizontal) windspeed
W_x, W_y	-	Horizonal windspeed components
x, y	-	Horizontal position coordinates of aircraft
x_c, y_c	-	Horizontal position coordinates of microburst center
α	-	Angle-of-attack
β	-	Throttle response
γ	-	Flight path angle
θ	-	Attitude
λ_s	-	Adjoint variable corresponding to state variable s
μ	-	Bank angle
ρ	-	Air density
τ	-	Time constant of throttle response
χ	-	Heading angle
χ_w	-	Horizontal wind direction

Subscripts

o	- initial value
c	- center of microburst
f	- final value
max	- maximum value
ref	- target value

Superscript

*	- optimal value

1. Introduction

Weather phenomena that cause windshear, in particular the so-called "microburst", present a significant safety hazard during the take-off and landing of an aircraft. Such a microburst is a strong downdraft that strikes the ground, producing winds that diverge radially from the impact point (see Fig. 1). An airplane which penetrates the center of a microburst in straight flight will initially experience an increasing headwind and consequent upward force. As the aircraft proceeds along the glide slope, the downdraft increases and the headwind shifts into a tailwind causing the aircraft to loose speed and altitude (see Fig. 2).

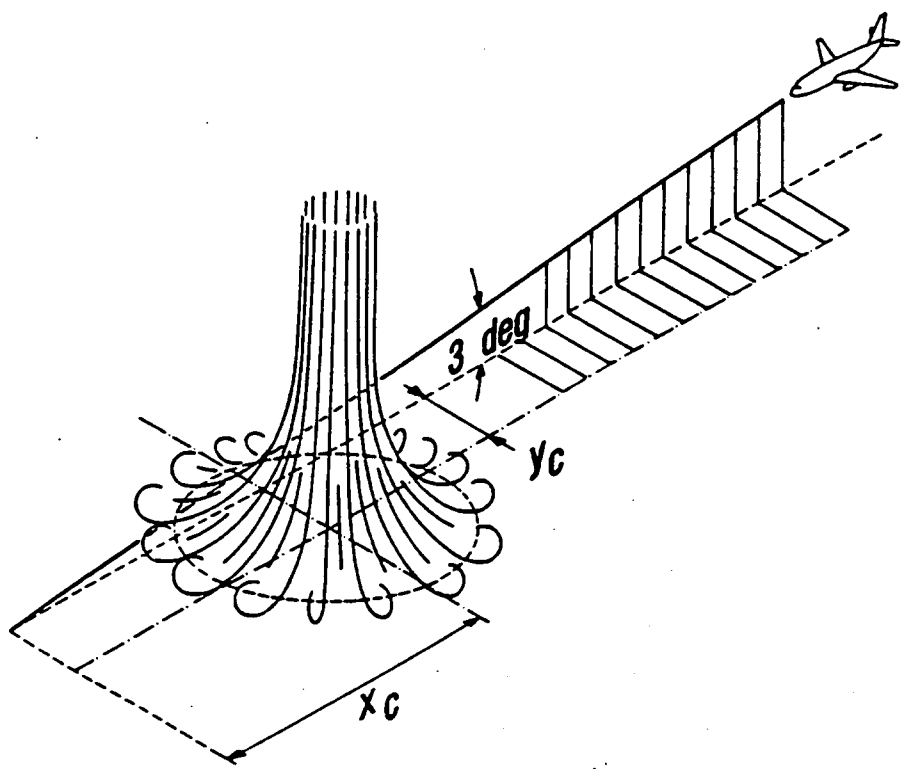

Figure 1 : Microburst encounter during final approach.

Reactive windshear warning systems, which are gradually becoming standard fit aboard modern jet airliners, are capable of detecting such hazardous situations. When during final approach an aircraft is flying along the glide slope and such a potentially dangerous windshear situation is detected at a sufficiently early stage, the pilot may abort the landing and initiate an escape maneuver.

Research efforts which aim at establishing the optimal control strategy for such escape procedures have been conducted for some time now[1]. However, most of these studies have focussed on controlling and optimizing flight trajectories in a vertical plane. Of particular interest in this context is the work of Miele et al. In addition to considering control strategies to improve the take-off and penetration landing performance during microburst encounter[2,3], Miele also specifically deals with the abort landing[4]. In Ref. 4 Miele et al. consider optimal (open-loop)trajectories through windshears and downdraft

that minimize the peak value of the altitude drop, as well as closed-loop guidance strategies that closely approximate these open-loop optimal trajectories.

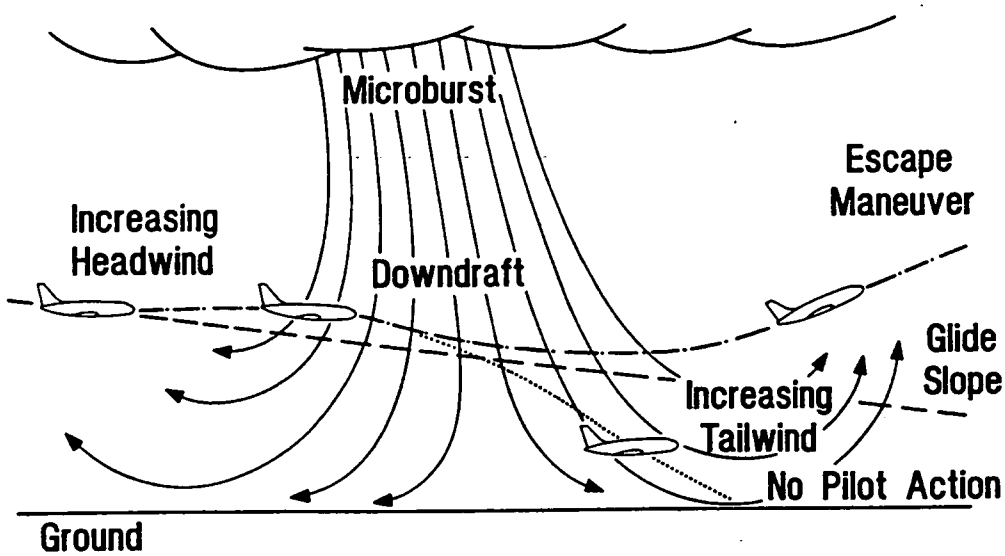

Figure 2 : Straight flight through a microburst.

In Refs. 5 and 6, Zhao and Bryson propose an alternative formulation for the optimization of flight paths through microbursts, using a different performance measure. More specifically, paths are determined through windshears and downdrafts that maximize the final value of specific energy, while taking into account a minimum altitude constraint. It turns out that for strong-to-severe microbursts, the computed optimal paths are not essentially different from those found by Miele. In both cases the optimal strategy is (i) to initially descend to the minimum altitude, (ii) to remain in the vicinity of that minimum altitude, and (iii) to ascend once the aircraft has passed through the shear region.

Other dynamic optimization and flight guidance studies of considerable interest include those performed by Psiaki and Stengel, and by Hinton. The extensive parametric investigations of Psiaki and Stengel[7,8] have been particularly aimed at achieving a broad understanding of the factors that most strongly affect a microburst recovery, including variations in the microburst characteristics. Hinton[9] has examined a set of candidate strategies for recovery from microburst encounter, using both batch and piloted simulation. His findings indicate that in piloted operations, the performance of advanced optimal guidance laws (such as those developed by Miele et al.) is not significantly better than the performance of simple strategies, such as the constant pitch technique. On the other hand, improving the alert time by just a few seconds was shown to lead to a significant performance increase. The above optimization studies clearly indicate that early detection and warning of dangerous windshear significantly increases the survivability during final approach. For this reason substantial research efforts are currently being undertaken to

develop so-called forward looking windshear detection systems which allow to look ahead of the aircraft[9,10]. In addition to improving the alert time, the availability of the information on the location of a microburst also offers the possibility of applying escape procedures involving lateral maneuvering. By turning the aircraft away from the microburst center, rather than flying straight through (see Fig. 3), the hazards caused by the penetration of a microburst can be reduced. These potential improvements were recently confirmed by a simulation study[11], in which flights with and without lateral maneuvering were compared. In this simulation study, the longitudinal strategy as recommended by the FAA Windshear training aid[12] was used, while lateral maneuvering was performed by commanding a constant bank angle of specified magnitude. Encouraged by these findings, the aim of the present study is to extend the work of Miele et al. by computing optimal abort landing trajectories that feature lateral maneuvering. The characteristics of these trajectories are analyzed for the purpose of developing near-optimal escape guidance strategies. The actual starting point for the present effort is the work reported in Ref. 1. Reference 1 documents the outcome of an effort to replicate the results of Miele et al. with some minor modifications in both model and problem formulations, but using a completely different numerical method.

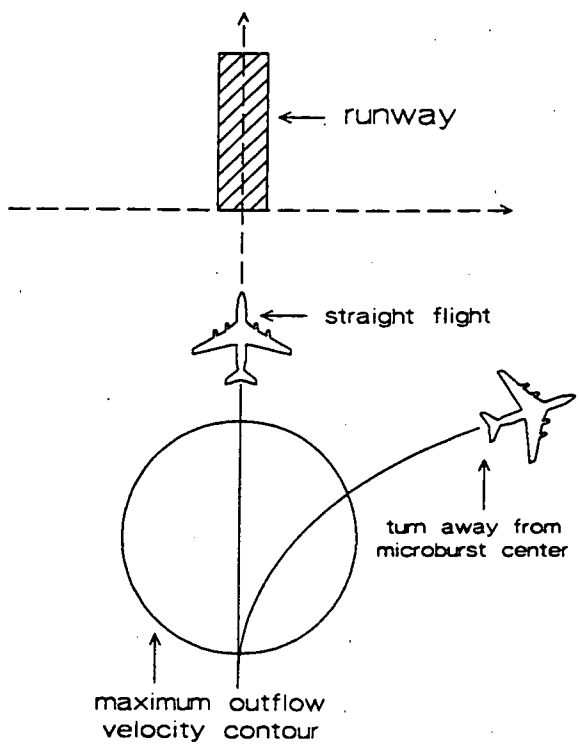

Figure 3 : Escape with and without lateral maneuvering.

In comparison to escape procedures which are restricted to flight in a vertical plane, the present formulation introduces an additional control variable, namely, bank angle. Although banking generally reduces the performance of an aircraft due to the required additional lift, banking may also lead to a "positional advantage" within the microburst flow field. In addition to establishing an optimal escape strategy, it will also be of considerable interest to investigate to what extent lateral and longitudinal dynamics are

actually coupled for such escape maneuvers.

2. Microburst Encounter Modeling

2.1 Equations of Motion

Using a relative wind-axes reference-frame, the equations of motion, describing the aircraft dynamics (represented by a point-mass model) in the three-dimensional space can be written as:

$$\dot{x} = V\cos\gamma\cos\chi + W_x \tag{1}$$

$$\dot{y} = V\cos\gamma\sin\chi + W_y \tag{2}$$

$$\dot{h} = V\sin\gamma + W_h \tag{3}$$

$$\dot{E} = \frac{(T-D)V}{W} + W_h - \frac{V}{g}[\dot{W}_x\cos\gamma\cos\chi + \dot{W}_y\cos\gamma\sin\chi + \dot{W}_h\sin\gamma] \tag{4}$$

$$\dot{\gamma} = \frac{g}{V}[\frac{L\cos\mu}{W} - \cos\gamma] + \frac{1}{V}[\dot{W}_x\sin\gamma\cos\chi + \dot{W}_y\sin\gamma\sin\chi - \dot{W}_h\cos\gamma] \tag{5}$$

$$\dot{\chi} = \frac{g}{V\cos\gamma}\frac{L\sin\mu}{W} + \frac{1}{V\cos\gamma}[\dot{W}_x\sin\chi - \dot{W}_y\cos\chi] \tag{6}$$

$$\dot{\beta} = \frac{1}{\tau}[\beta_t - \beta] \tag{7}$$

where x, y and h are the position coordinates, E is the specific energy, γ is the flight path angle, χ is the heading angle and β the throttle response. The wind velocity vector has three components, viz., W_x, W_y and W_h. The above equations embody the following assumptions: (i) a flat non-rotating earth, (ii) thrust T is aligned with the airspeed vector, (iii) the wind flow field is steady, (iv) the aircraft weight is constant. The throttle response is modeled as a first-order lag with a time constant τ. Note that since specific energy E is used here as a state variable, the airspeed V should be merely regarded as a function of energy E and altitude h, to be obtained from the relation:

$$E = h + \frac{V^2}{2g} \tag{8}$$

In the mathematical model the controls are:

(i) The throttle setting β_t constrained by:

$$0 \leq \beta_t \leq 1 \tag{9}$$

(ii) The bank angle μ which is limited by:

$$|\mu| \leq \mu_{max} \tag{10}$$

(iii) The angle-of-attack α which is forced to remain within the range:

$$0 \leq \alpha \leq \alpha_{max} \tag{11}$$

The aerodynamic forces (lift L and drag D) are functions of airspeed V, altitude h and the angle-of-attack α:

$$L = C_L(\alpha)\frac{\rho V^2 S}{2} \tag{12}$$

$$D = C_D(\alpha)\frac{\rho V^2 S}{2} \tag{13}$$

Since the trajectories under investigation involve relatively modest variations in altitude, the maximum thrust is assumed to be a function of airspeed only, i.e.:

$$T = \beta T_{max}(V) \tag{14}$$

Although the aim of the present work is to extend the work of Miele et al. to flight in three dimensions, there are some slight modifications incorporated in the current model, relating to the throttle and angle-of-attack dynamics. In the work of Miele et al. not only a bound is imposed on the maximum value the angle-of-attack α can attain, but also the rate of change of this variable is limited. In order to enforce these constraints indirectly, Miele et al. use a transformation technique that results in a system model in which the angle-of-attack has acquired the status of state variable. Moreover, an auxiliary variable, which

essentially controls the rate of change of the angle-of-attack, is introduced to replace angle-of-attack as the control variable. Since in the present study we have ***not*** imposed such an upper limit on the rate of change of the angle-of-attack, the angle-of-attack can continue to serve as a control variable in the system model. However, it needs to be realized that the current assumption of an ***instantaneous*** angle-of-attack response is indeed fairly unrealistic in performance studies of the type considered here and a critical review of the basic assumptions is therefore clearly warranted in future research. Incidentally, the present assumption of an instantaneous bank angle response clearly should be included in such a "refinement process".

Another simplification in the present study relates to the already mentioned assumption that the thrust T is aligned with the airspeed vector. Clearly, this assumption is questionable for maneuvers in which high angles of attack are employed. For the microburst escape maneuvers considered here this may indeed be the case. However, a comparison of simulated (constant pitch) guidance solutions revealed that, although performance is affected by the assumption, the characteristic behavior of the escape maneuvers based on the equations of motion (1) through (7) is not significantly different from maneuvers which are computed on the basis of equations of motion in which the thrust T has a fixed direction relative to the body-axis system of the aircraft. Also with respect to this particular issue, it will be relatively simple to modify the system model in future research.

In the abort landing study of Miele et al.[4] the throttle response is not modeled as a first order lag, but rather as "ramp function". This slight difference in modeling approach is not expected to lead to a significantly different behavior.

2.2 Aerodynamic and Thrust Characteristics

In this study a Boeing 727 point-mass model has been used, that has been adapted from a model originally developed by Miele et al.[2,3,4]. The main characteristics of this aircraft model are:

$$T_{max} = T_0 + T_1 V + T_2 V^2 \tag{15}$$

$$C_D = D_0 + D_1 \alpha + D_2 \alpha^2 \tag{16}$$

$$C_L = L_0 + L_1 \alpha + L_2 (\alpha - \alpha_{ref})^2 \tag{17}$$

Details of the aerodynamic and thrust data are summarized in Table 1.

Table 1 : aerodynamic and thrust data of the B-727 aircraft model.

W	$= 667233$ N , $S = 144.9$ m^2 , $\tau = 3$ sec	
T_0	$= 198280$ N	
T_1	$= -350.08$ N(m/s)$^{-1}$	
T_2	$= 0.69063$ N(m/s)$^{-2}$	
D_0	$= 0.15751$	
D_1	$= 0.0768$ rad^{-1}	
D_2	$= 2.524$ rad^{-2}	
L_0	$= 0.7076$	
L_1	$= 5.97$ rad^{-1}	
L_2	$= 0$	if $0 \leq \alpha \leq \alpha_{ref}$
	$= -5.95$ rad^{-2}	if $\alpha_{ref} \leq \alpha \leq \alpha_{max}$
α_{ref}	$= 0.2269$ rad	
α_{max}	$= 0.3002$ rad	

2.3 The Microburst Wind Model

The microburst model used herein is an axisymmetric three-dimensional extension of the two-dimensional model presented in Ref. 1. Due to the axisymmetric character of the microburst model, it is convenient to use polar coordinates to describe the flow field in a horizontal plane (see Fig. 4). The employed analytic approximation of the flow field characteristics actually features separate models for the radial flow (which may lead to horizontal shear) and the downdraft. The induced radial and vertical wind velocities at any point in the three-dimensional space can be computed through the following relations:

$$W_r = f_r\left[\frac{100}{\left(\frac{r - D/2}{200}\right)^2 + 10} - \frac{100}{\left(\frac{r + D/2}{200}\right)^2 + 10}\right] \qquad (18)$$

$$W_h = -f_h\left[\frac{0.4h}{(\frac{r}{400})^4 + 10}\right] \quad , \tag{19}$$

where r is the radial distance from the microburst center (axis of symmetry) located at the point (x_c, y_c), i.e.:

$$r = \sqrt{(x - x_c)^2 + (y - y_c)^2} \tag{20}$$

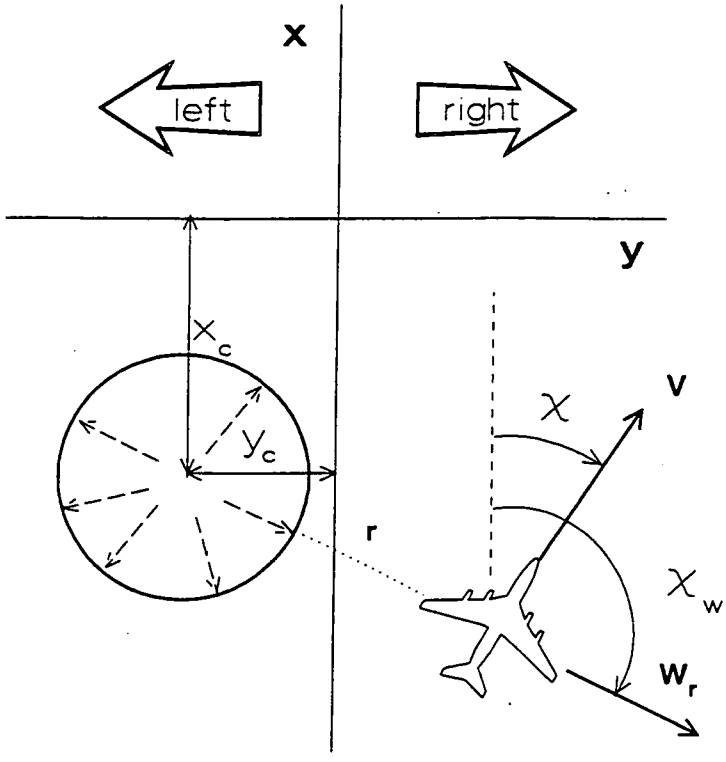

Figure 4 : Geometry of microburst encounter.

Note that in the present study the origin of the coordinate frame is located at the runway threshold. The parameter D in Eq. (18) specifies the diameter of the peak radial outflow-velocity contour (in this study D is always taken as 2000 m). The parameters f_r and f_h characterize the intensity of the horizontal shear and downdraft respectively. This implies that not only the absolute strength of the burst can be a priori selected, but also the relative strength of the horizontal and vertical winds components can be changed if desired. However, in all examples presented in this work the parameters f_r and f_h have been set at the value 2. The wind profiles corresponding to the model given in Eqs.(18) and (19) are shown in Fig. 5, for the above indicated values of the parameters. Note that

the horizontal wind component W_r is only a function of the radial distance to the microburst center, whereas the vertical wind component W_h also depends on altitude to ensure that W_h decreases with decreasing altitude and satisfies the continuity condition, i.e. zero vertical windspeed at ground level. Clearly, the vertical windspeed model (at least in the neighborhood of the microburst center) is valid at low altitudes only.

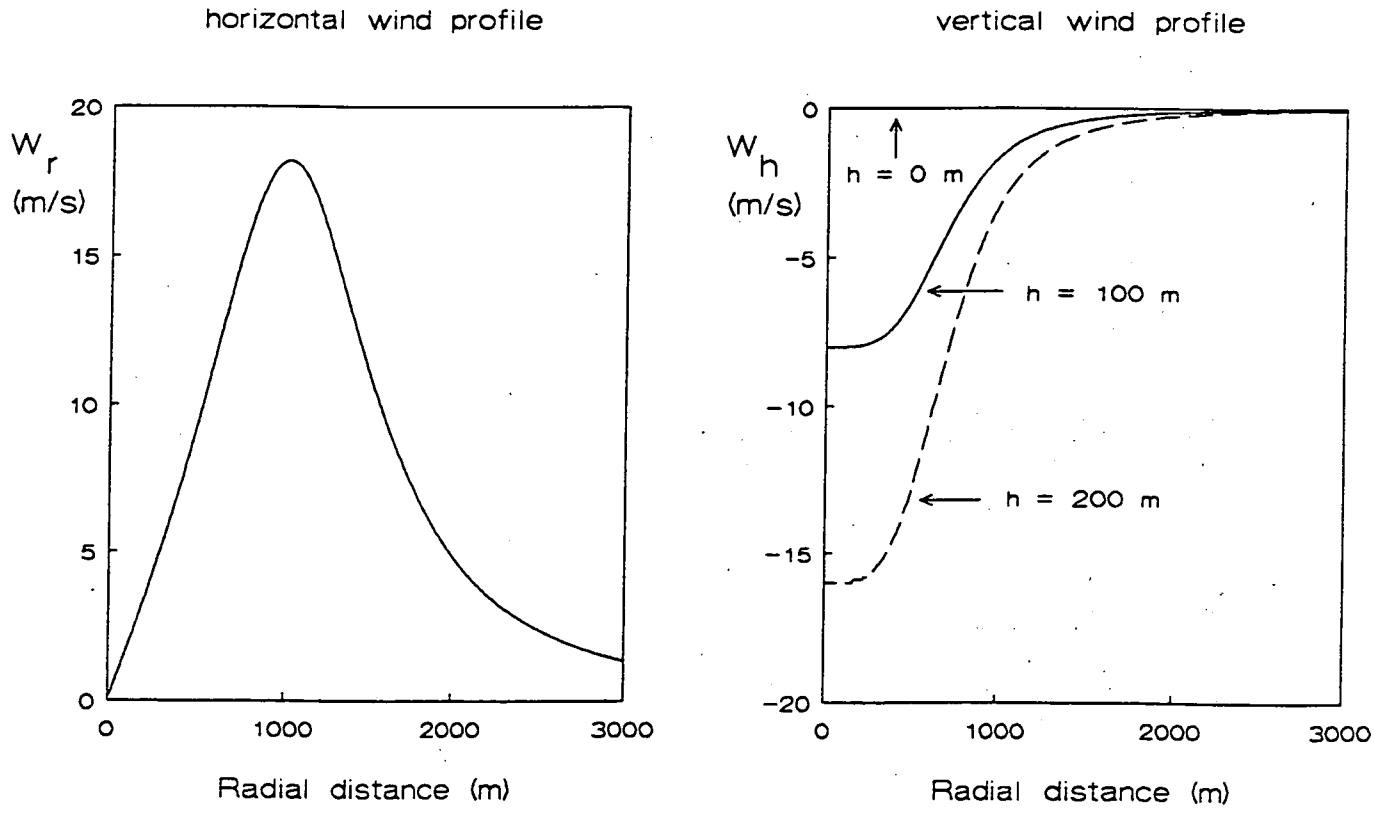

Figure 5 : Horizontal and vertical wind velocity profiles

The wind model given by Eqs.(18) and (19) differs from the model used by Miele et al.[2,3,4]. The present model has the (mathematical) advantage that it is very smooth.

Using polar coordinates, the horizontal wind components W_x and W_y can be readily related to the radial windvelocity W_r:

$$W_x = \cos\chi_w W_r(r) \quad ; \quad W_y = \sin\chi_w W_r(r) \quad , \tag{21}$$

where χ_w is the direction of the radial wind velocity vector. In view of assumption (iii) in the previous Section, the total derivatives of these wind velocity components satisfy the relations:

$$\dot{W}_x = \frac{\partial W_x}{\partial x}\dot{x} + \frac{\partial W_x}{\partial y}\dot{y} \quad ; \quad \dot{W}_y = \frac{\partial W_y}{\partial x}\dot{x} + \frac{\partial W_y}{\partial y}\dot{y} \tag{22}$$

$$\dot{W}_h = \frac{\partial W_h}{\partial x}\dot{x} + \frac{\partial W_h}{\partial y}\dot{y} + \frac{\partial W_h}{\partial h}\dot{h} \tag{23}$$

An important characteristic parameter used in the evaluation of windshear performance is the so-called Bowles F-factor. Here we define this windshear hazard factor as:

$$F \triangleq \frac{(T-D)}{W} - \frac{\dot{E}}{V} \tag{24}$$

Defining the F-factor in this particular fashion permits its use in the analysis of both two-dimensional and three-dimensional windshear encounters. A Comparison of Eqs.(4) and (24) reveals that the F-factor can be readily interpreted as the loss or gain in available excess thrust-to-weight ratio due to the combined effect of downdraft and horizontal windshear. The F-factor therefore represents a direct measure of the degradation of an aircraft's climb gradient capability at constant speed caused by the presence of windshear/downdraft. Note that positive values of the F-factor indicate a performance decreasing situation. Substitution of Eq.(4), combined with the use of polar horizontal position coordinates, allows the F-factor in Eq.(24) to be conveniently expressed as:

$$\begin{aligned} F = {} & \frac{\cos\gamma}{g}\{V\cos\gamma[\frac{\partial W_r}{\partial r}\cos^2(\chi-\chi_w) + \frac{W_r}{r}\sin^2(\chi-\chi_w)] + W_r\frac{\partial W_r}{\partial r}\cos(\chi-\chi_w)\} \\ & + \frac{\sin\gamma}{g}\{\frac{\partial W_r}{\partial r}[W_r + V\cos\gamma\cos(\chi-\chi_w)] + \frac{\partial W_h}{\partial h}[W_h + V\sin\gamma]\} - \frac{W_h}{V} \end{aligned} \tag{25}$$

In the derivation of Eq.(25) use is made of the partial derivatives evaluated in Appendix A. Appendix A also presents the equations of motion written in polar coordinates.

It is noted that the F-factor does not merely depend on the spatial location within the flow field, but rather on all state variables. In Fig. 6 the F-factor is plotted as a function of the radial distance r and the "wind incidence angle" (χ_w - χ), using values for altitude, speed and flight path angle, representative of a final approach. It is observed that for the present wind model the peak value of the F-factor is not generally reached at the center of the microburst, but rather at some distance away from the center. It can also be seen that an energy gain due to windshear is also possible. However, from Fig. 6 it is readily clear that this can never be the case if the wind incidence angle (χ_w - χ) is 90°. When an aircraft is flying well outside the peak radial outflow-velocity contour, the best performance is achieved by flying along a "***wind radial***".

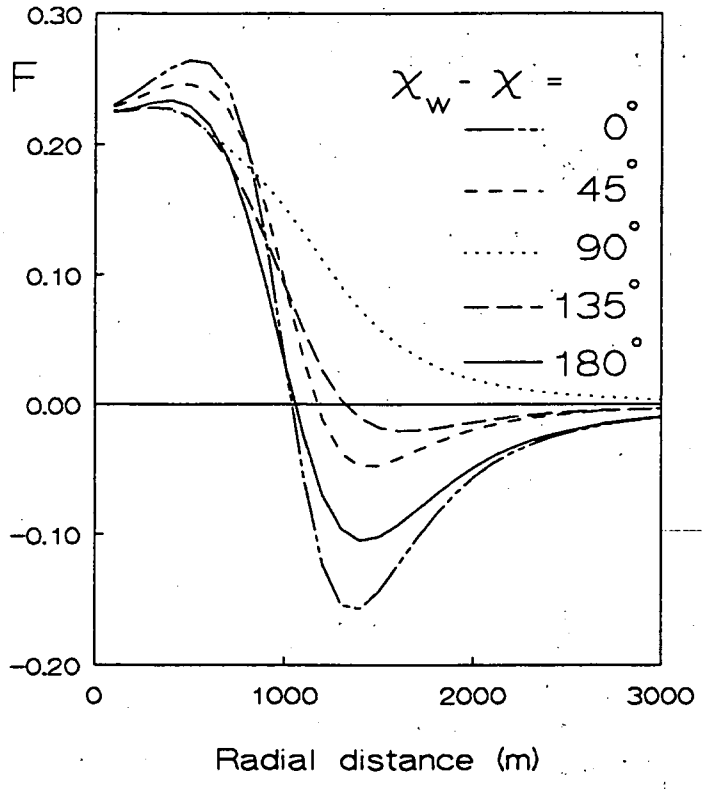

Figure 6: The F-factor as a function of the radial distance r, for several values of the wind incidence angle $\chi_w - \chi$, where it is assumed that V = 70 m/s, h = 100 m and $\gamma = -3°$.

3. Optimal Control Formulation

3.1 Optimization Criterion

Similar to Ref.4, the objective in this study is to maximize the minimum altitude reached by an aircraft at any point along the trajectory, or, in other words, to minimize the peak value of the altitude drop (see Fig. 7):

$$I^* = \min I = \min \left[\max_t \left(h_{ref} - h(t) \right) \right] \tag{26}$$

Following the approach of Ref.4, the minimax criterion in Eq.(26) (Chebyshev performance index), is ***approximated*** by a Bolza performance index:

$$J^* = \min J = \min \int_0^{t_f} (h_{ref} - h)^n \, dt \quad , \tag{27}$$

where n is a large positive, even exponent. Note that for the best possible computational results, the reference altitude h_{ref} should be chosen as small as possible, but such that the right-hand side of Eq.(26) remains positive at all times. The numerical values of the constants in Eq.(27) that have been used here are: n = 6 and h_{ref} = 400 m.

It is noted that in addition to the above ***approximation***, it is also possible to apply another transformation technique which can solve the ***original*** minimax problem (26). More specifically, the minimax problem can be converted into an equivalent optimal control problem with state variable inequality constraints[15,16]. In conjunction with the presently used multiple-shooting algorithm, this technique appears to be particularly suited for numerical treatment of the Multiple-Boundary-Value-Problem which arises from the optimal control analysis. Although this approach is mathematically extremely complicated, it definitely merits further consideration in future research.

3.2 Boundary Conditions

The following initial conditions (at which the escape procedure is commenced) have been assumed in this study:

$x(0) = x_0 = -2500$ m , $\quad y(0) = y_0 = 0$ m ,

$h(0) = h_0 = 131$ m , $\quad E(0) = E_0 = 384.326$ m ,

$\gamma(0) = \gamma_0 = -3°$, $\quad \chi(0) = \chi_0 = 0°$,

$\beta(0) = \beta_0 = 0.333$

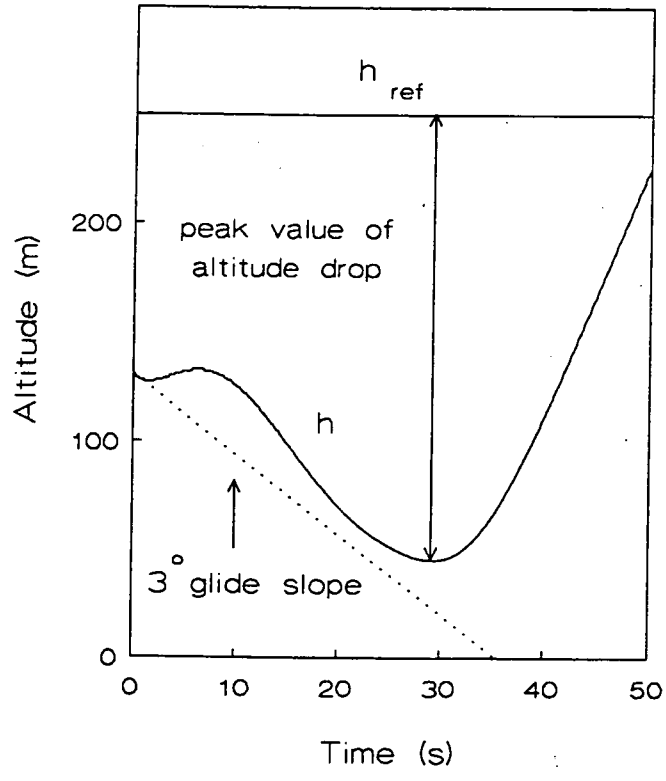

Figure 7 : Illustration of Performance Index

These values correspond to a situation in which an aircraft would fly during a stabilized approach (V = 70.5 m/s) without winds or windshear. It needs to be realized that in the presence of winds, the required values for γ and β will be somewhat different. However, since different locations of the microburst will be considered in the numerical examples, the above stated values will be assumed to apply in all situations, merely to achieve some degree of consistency. The final time t_f has been set to 50 seconds, which is sufficiently long to allow a transition of the shear region. No terminal boundary conditions have been imposed. Such conditions would mainly affect the extremal solution in the after-shear region. Our primary interest is in the control behavior during the passage of the shear region.

3.3 Necessary Conditions for Optimality

To summarize, the optimal control problem to be solved is to determine the optimal controls β^*, μ^* and α^* such that starting from the initial conditions, the performance index of Eq.(27) is minimized for a given final time t_f.

In the following the first-order necessary conditions for optimality[13] are given. First, the variational Hamiltonian of the problem is defined as:

$$
\begin{aligned}
H = & -(h_{ref}-h)^n \\
& + \lambda_x\{V\cos\gamma\cos\chi + W_x\} + \lambda_y\{V\cos\gamma\sin\chi + W_y\} + \lambda_h\{V\sin\gamma + W_h\} \\
& + \lambda_E\{\frac{(T-D)V}{W} + W_h - \frac{V}{g}[\dot{W}_x\cos\gamma\cos\chi + \dot{W}_y\cos\gamma\sin\chi + \dot{W}_h\sin\gamma]\} \\
& + \lambda_\gamma\{\frac{g}{V}[\frac{L\cos\mu}{W} - \cos\gamma] + \frac{1}{V}[\dot{W}_x\sin\gamma\cos\chi + \dot{W}_y\sin\gamma\sin\chi - \dot{W}_h\cos\gamma]\} \\
& + \lambda_\chi\{\frac{g}{V\cos\gamma}\frac{L\sin\mu}{W} + \frac{1}{V\cos\gamma}[\dot{W}_x\sin\chi - \dot{W}_y\cos\chi]\} + \lambda_\beta\{\frac{1}{\tau}[\beta_c - \beta]\}
\end{aligned}
\tag{28}
$$

The system of adjoint equations and corresponding transversality conditions arises from the necessary conditions for optimality:

$$\dot{\lambda}_x = -\frac{\partial H}{\partial x} \quad ; \quad \lambda_x(t_f) = 0 \tag{29}$$

$$\dot{\lambda}_y = -\frac{\partial H}{\partial y} \quad ; \quad \lambda_y(t_f) = 0 \tag{30}$$

$$\dot{\lambda}_h = -\frac{\partial H}{\partial h}|_E = -\frac{\partial H}{\partial h}|_V + \frac{g}{V}\frac{\partial H}{\partial V}|_h \quad ; \quad \lambda_h(t_f) = 0 \tag{31}$$

$$\dot{\lambda}_E = -\frac{\partial H}{\partial E}|_h = -\frac{g}{V}\frac{\partial H}{\partial V}|_h \quad ; \quad \lambda_E(t_f) = 0 \tag{32}$$

$$\dot{\lambda}_\gamma = -\frac{\partial H}{\partial \gamma} \quad ; \quad \lambda_\gamma(t_f) = 0 \tag{33}$$

$$\dot{\lambda}_\chi = -\frac{\partial H}{\partial \chi} \quad ; \quad \lambda_\chi(t_f) = 0 \tag{34}$$

$$\dot{\lambda}_\beta = -\frac{\partial H}{\partial \beta} \quad ; \quad \lambda_\beta(t_f) = 0 \tag{35}$$

Note that the transversality conditions result in a zero terminal value for all the adjoints as a consequence of the fact that no terminal boundary conditions on the state variables have been imposed. Also note that the Appendix presents a complete overview of all the partial derivatives needed to evaluate the right-hand-sides of Eqs.(29) through (35).

The optimal control functions μ^* and α^* are found by applying the ***Maximum Principle***. Assuming these "optimal aerodynamic controls" are within the interior of their admissible range, the following conditions apply:

$$\frac{\partial H}{\partial \mu} = -\lambda_\gamma \frac{g}{V}\frac{L\sin\mu}{W} + \lambda_\chi \frac{g}{V\cos\gamma}\frac{L\cos\mu}{W} = 0 \;\Rightarrow\; \tan\mu = \frac{(\lambda_\chi/\cos\gamma)}{\lambda_\gamma} \tag{36}$$

$$\frac{\partial H}{\partial \alpha} = \lambda_\gamma \frac{g}{V}\frac{\rho V^2 S}{2W}\cos\mu\,\frac{\partial C_L}{\partial \alpha} + \lambda_\chi \frac{g}{V\cos\gamma}\frac{\rho V^2 S}{2W}\sin\mu\,\frac{\partial C_L}{\partial \alpha} - \lambda_E \frac{\rho V^3 S}{2W}\frac{\partial C_D}{\partial \alpha} = 0 \;, \tag{37}$$

where from Eqs.(16) and (17) it follows that:

$$\frac{\partial C_L}{\partial \alpha} = L_1 + 2L_2(\alpha - \alpha_{ref}) \;,\quad \frac{\partial C_D}{\partial \alpha} = D_1 + 2D_2\alpha \tag{38}$$

Let us define $\Phi(\mu)$ as:

$$\Phi(\mu) \triangleq \lambda_\gamma\cos\mu + (\lambda_\chi/\cos\gamma)\sin\mu \tag{39}$$

Substitution of Eqs.(38) and (39) into Eq.(37) allows to solve for α:

$$\alpha = \frac{\lambda_E D_1 (V^2/g) - [L_1 - 2L_2\alpha_{ref}]\Phi}{-2\lambda_E D_2 (V^2/g) + 2L_2\Phi} \tag{40}$$

It needs to be realized that the control solution of Eq.(36) is ambiguous in the sense that it has multiple roots. The Legendre-Clebsch Condition can be used to solve this ambiguity. In particular, for a maximum we must have that:

$$\frac{\partial^2 H}{\partial \mu^2} = -\frac{g}{V}\frac{L}{W}[\lambda_\gamma\cos\mu + (\lambda_\chi/\cos\gamma)\sin\mu] = -\frac{g}{V}\frac{L}{W}\Phi \le 0 \;\Rightarrow\; \Phi \ge 0 \;, \tag{41}$$

where $\Phi \ge 0$ must apply since physically it is clear that $L \ge 0$. From Eq.(36) it can be seen that:

$$\tan^2\mu = -1 + \frac{1}{\cos^2\mu} = \frac{(\lambda_\chi/\cos\gamma)^2}{\lambda_\gamma^2} \quad \Rightarrow$$

$$\cos^2\mu = \frac{\lambda_\gamma^2}{(\lambda_\chi/\cos\gamma)^2 + \lambda_\gamma^2} \quad ; \quad \sin^2\mu = \frac{(\lambda_\chi/\cos\gamma)^2}{(\lambda_\chi/\cos\gamma)^2 + \lambda_\gamma^2} \tag{42}$$

The appropriate roots of Eqs.(42) are:

$$\cos\mu = \frac{\lambda_\gamma}{\sqrt{(\lambda_\chi/\cos\gamma)^2 + \lambda_\gamma^2}} \quad ; \quad \sin\mu = \frac{(\lambda_\chi/\cos\gamma)}{\sqrt{(\lambda_\chi/\cos\gamma)^2 + \lambda_\gamma^2}} \quad , \tag{43}$$

which can be readily verified by substitution of Eq.(43) into eq.(41):

$$\Phi = \sqrt{(\lambda_\chi/\cos\gamma)^2 + \lambda_\gamma^2} \geq 0 \tag{44}$$

If the control constraints in Eqs.(10) and (11) are taken into account, the optimal control solutions μ^* an α^* are ultimately given by:

$$\mu^* = \min\{\mu_{max}, |\arctan[\frac{(\lambda_\chi/\cos\gamma)}{\lambda_\gamma}]|\} \cdot sign(\lambda_\chi) \tag{45}$$

$$\alpha^* = \max\{0, \min[\alpha_{max}, \frac{\lambda_E D_1(V^2/g) - [L_1 - 2L_2\alpha_{ref}]\Phi(\mu^*)}{-2\lambda_E D_2(V^2/g) + 2L_2\Phi(\mu^*)}]\} \tag{46}$$

The third control variable is the throttle setting β_t. Again, from physical considerations it is clear that full throttle should be applied during a microburst escape maneuver. Mathematically this fact needs to be checked by verifying that:

$$\lambda_E \geq 0 \tag{47}$$

The above stated Two-Point-Boundary-Value-Problem (TPBVP) consisting of the 7 state equations and 7 adjoint equations, is of considerable mathematical complexity. In the present study the extremals (solutions to the TPBVP) have been obtained iteratively using a highly accurate ***multiple-shooting algorithm***[14]. At this point it is important to note, however, that such extremal solutions are merely candidates for local optimality. As a matter of fact, we have been able to find up to three extremals for a given set of boundary conditions in most cases. It is imperative to verify local optimality of these candidate extremals, by checking for the second-order necessary conditions (Jacobi-test). Such a test, together with the Legendre-Clebsch condition (which is easily verified) can provide

assurance concerning the local optimality of candidate extremals. We emphasize, however, that, as yet, we have only concerned ourselves with computing candidate extremals.

4. Extremal Solutions

4.1 Reference Solution

In order to investigate the characteristic features of the optimal escape trajectories, the principal parameters that have been varied in this study are the position coordinates (x_c, y_c) of the microburst center. The reference situation that has been selected to serve as a baseline concerns a microburst of which the center is located at (-1500 m, 0 m). This implies that for the given initial conditions, an aircraft in straight flight will fly exactly along the x-axis of the reference frame (see Fig.4), passing right through the microburst center. Relative to this "symmetric" reference situation both the distance of the microburst center to the runway threshold (x_c-coordinate position) and the lateral offset distance y_c have been varied within the range [-500 m, +500 m]. It is noted that extending this range is of limited value in the sense that such an extension will result in a situation which is either not survivable or does not pose a real safety hazard. Moreover, such an extension may also lead to numerical complications, as will be discussed below.

In the Figs. 8 the results pertaining to the reference situation have been summarized. Due tot he symmetry in the geometry of this microburst-encounter, it is not really surprising that the first converged extremal that was obtained simply was the optimal trajectory established earlier in the two-dimensional analysis[1], i.e. a straight flight along the x-axis, during which an aircraft does not experience any cross-wind. Initial efforts to compute lateral escape trajectories were unsuccessful in the sense that the TPBVP solutions failed to converge. It soon turned out that the only way in which lateral escape trajectories could be generated at all, was by specifying a fairly low value for the bank angle limit μ_{max}. Indeed, for most of the considered encounters the maximum bank angle limit that can be specified is typically in the order of 15°. At this stage, it is suspected that one of the main reasons for the lack of convergence of the algorithm for higher values of the bank angle limit is related to the presently used Bolza performance index, as defined in Section 3.1 (recall that altitude should remain below the specified value of h_{ref} at all times). As a matter of fact, by increasing the value of h_{ref} in Eq.(27) from 400 m to 450 m, we have been able to obtain converged solutions for a bank angle limit exceeding 15°. Unfortunately, this measure had a rather adverse impact on the accuracy of the extremal solutions, in the sense that it resulted in a considerably lower minimum altitude. It is clear that in order to be able to perform a parametric study in which extremal solutions for different locations of the microburst are compared, the parameters in the Bolza performance index given by Eq.(27) must be uniquely defined. For the present study the selection of parameters as presented in Section 3.1, therefore represents a compromise between trajectory accuracy and the ability to perform a meaningful parametric investigation.

To demonstrate the impact of the bank angle limit on the solution behavior, three different values for the bank angle limit have been considered in Figs. 8, namely 5°, 10° and 15°. Moreover, due to symmetry considerations it is clear that lateral escape maneuvers can be performed by making either a left or a right turn. Consequently, it can be concluded that for any given (non-zero) value of the bank angle limit, three different extremals can be found (left turn, right turn, straight flight).

Figure 8a shows the ground tracks for the escape maneuvers. It is noted that for the considered reference situation, the location of the microburst center is such that the initial conditions for the trajectories are on the maximum radial outflow velocity contour.

Figures 8b and 8c show the time-histories for the two control variables, angle-of-attack and bank angle. As mentioned earlier, it is evident that all escape maneuvers are performed at full throttle and for this reason no plots for this third control variable have been included in this report. The most striking feature in the observed angle-of-attack behavior is that in all cases about the same minimum value is reached at about the same time. The higher the specified bank angle limit, the higher the initial angle-of-attack, while the angle-of-attack limit is also reached earlier. With respect to bank angle behavior, it can be observed that nearly all turning takes place in the initial phase. At some instance bank angle leaves its limit and decays to zero. The higher the value of the maximum bank-angle the earlier this decay sets in.

The behavior demonstrated by the turning extremals is fairly transparent. The relatively high initial angle-of-attack for a lateral maneuver results in a relatively high lift and drag. Due to the rather modest values of the bank angle limit, the increase in lift does not only lead to a high turn rate, but it also results in an initial "***zoom climb***", as can be observed in Figure 8d. In this initial (turning) phase, airspeed is reduced (see Fig. 8g) which actually helps to counter the increase in drag. Clearly, an initial high turn rate is desired to direct the aircraft away from the microburst center, such as to obtain a positional advantage within the wind flow field. On the other hand, it is also desirable to keep the energy bleed-off rate (and thus drag) as modest as possible. The optimization process attempts to establish the overall best compromise between those two conflicting requirements.

It is noted that there is a close correspondence between the angle-of-attack behavior and the F-factor behavior (Fig. 8e). For example, maximum angle-of-attack is generally reached at the end of shear region (region with high F-values). In Ref. 10 a microburst is classified as hazardous if the average F-factor exceeds .1 over any 1 km segment. Using this as a yardstick, it is readily clear that the microburst encounter considered here easily qualifies as hazardous. Figure 8e also shows that turning the aircraft away from the microburst center does not necessarily lead to a reduction in the peak value of the F-factor, but rather the shear region is passed much quicker.

Figure 8f shows the typical behavior of the corresponding heading angle time-history for one extremal. Generally speaking it can be observed that in the final stage of an escape maneuver, an aircraft ends up flying along a "horizontal wind radial". For a lateral escape maneuver this alignment takes place in the after-shear region. The F-factor plot shown in Fig. 6, along with the associated comment in Section 2.3, help to provide insight into this particular behavior.

Figure 8g compares the airspeed behavior of escape trajectories with and without lateral maneuvering. Although in the initial phase the airspeed is lower for the lateral escape maneuver, specific energy is actually well-managed in this maneuver. At termination, the airspeed for both trajectories is about the same, but the altitude for the lateral escape trajectory is significantly higher, implying that specific energy is higher.

The improvements in performance that can be obtained by executing a lateral escape maneuver are significant, as can be observed from Fig. 8d. The minimum altitude reached at any point along the trajectory has been plotted as a function of the specified bank angle limit in Fig. 8h (the curve labeled exact solution). The results clearly indicate that even better results can be expected for higher values of the specified bank angle limit. As already mentioned earlier, we have as yet not been able to obtain such solutions.

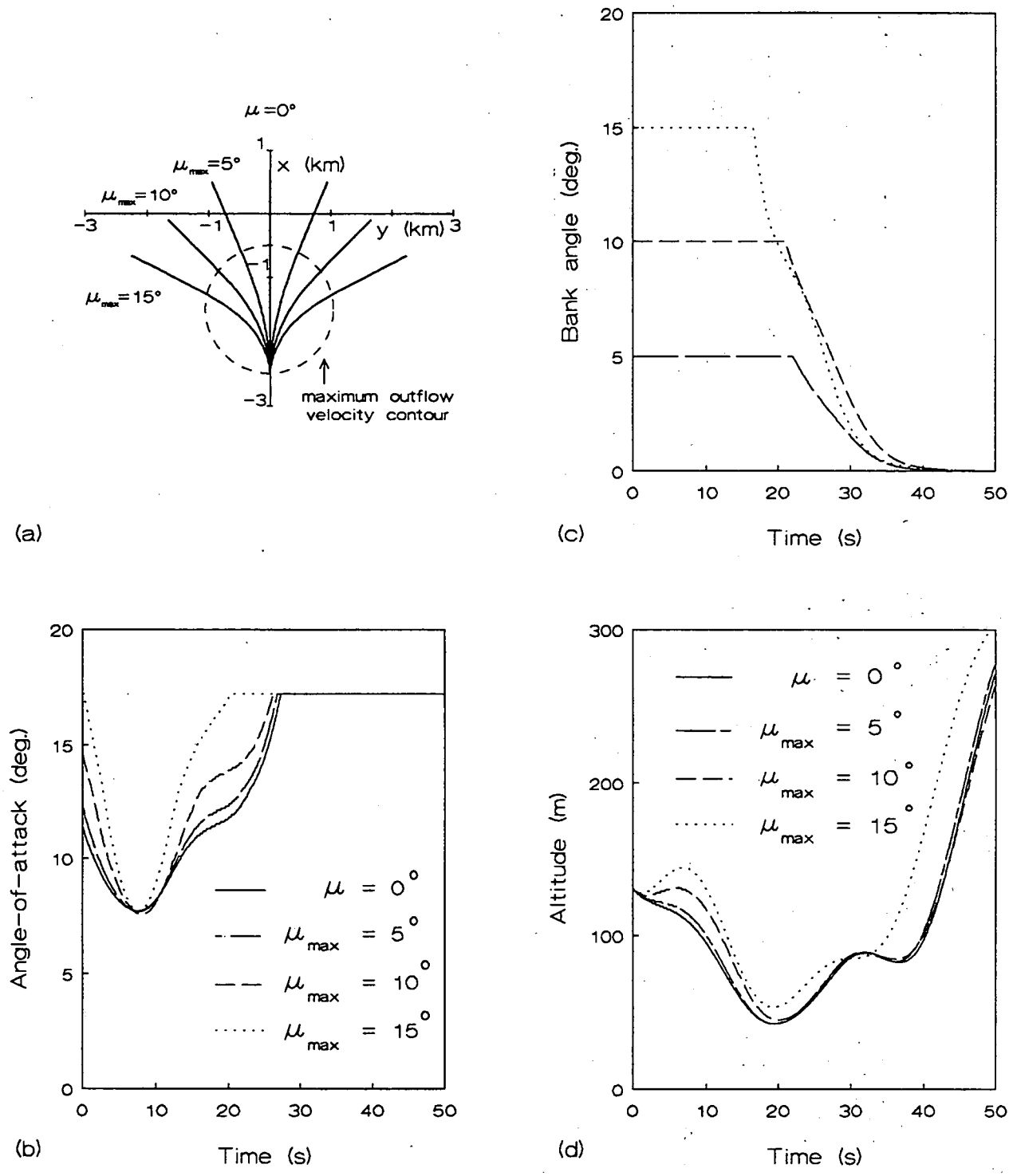

Figure 8 : Comparison of extremal solutions for various values of the bank angle limit (reference solution). Distance of the microburst center to the runway threshold is 1500 m. No lateral displacement.

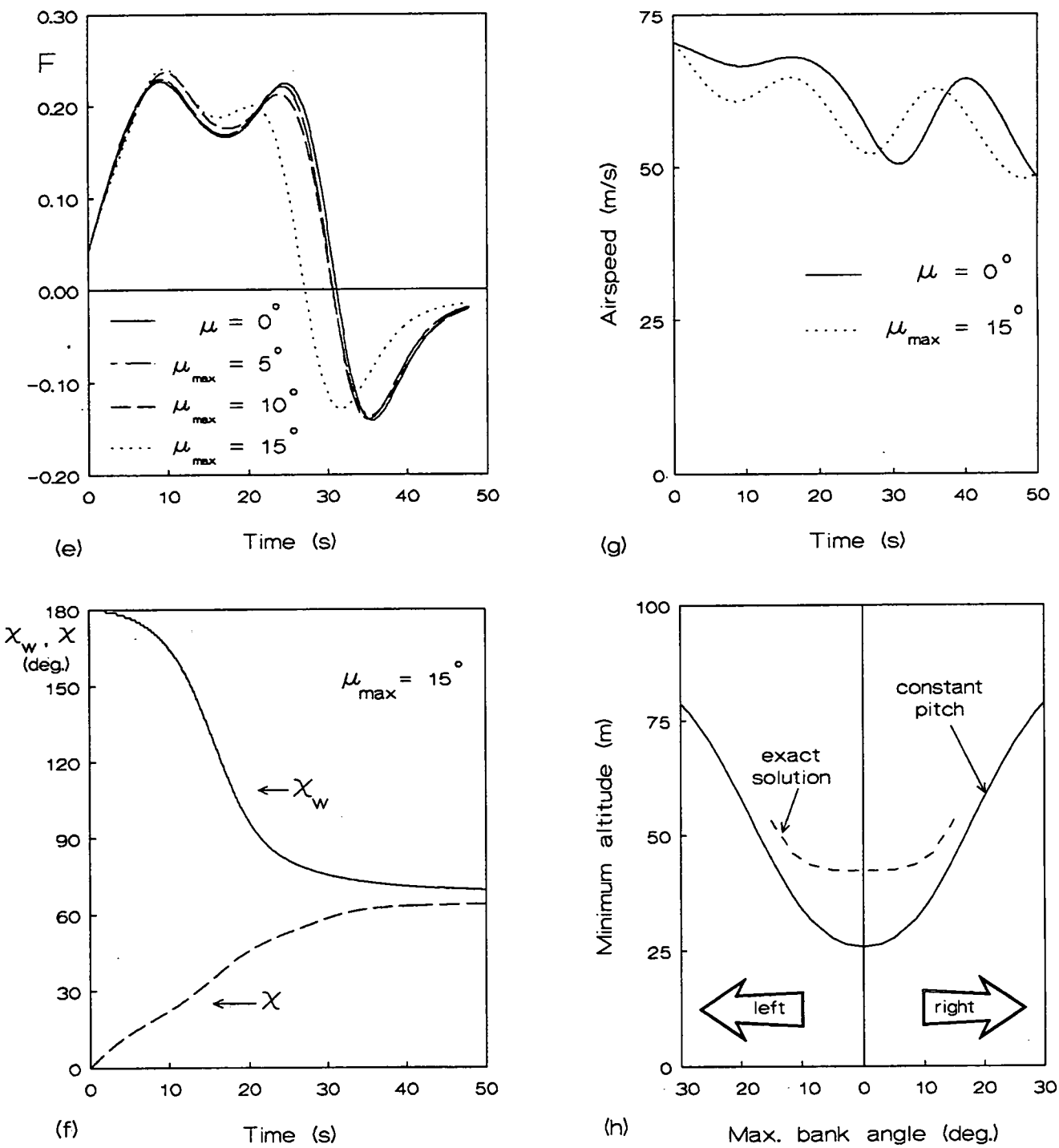

Figure 8 : (continued) Comparison of extremal solutions for various values of the bank angle limit (reference solution). Distance of the microburst center to the runway threshold is 1500 m. No lateral displacement.

4.2 Effect of a Lateral Microburst Displacement

A second numerical example of extremal behavior concerns a situation in which the center of the microburst is offset from the x-axis of the reference frame. In this particular example, the lateral microburst displacement y_c is set to 100 m. The results are illustrated in Figs. 9. The ground tracks shown in Fig. 9a do no longer exhibit a symmetry relative to the x-axis. In other words, there is now a need to distinguish between left and right turns. However, we still have the situation that there are generally three different extremals for a given value of the bank angle limit (provided this value is sufficiently large, as will be shown).

First of all, there is an extremal, which, like in the reference solution, passes right through the microburst center. This extremal has been labeled "***unconstrained***", to indicate that only some modest initial banking is required (see Fig. 9c). A second type of extremals concerns escape trajectories involving a turn to the right, or, in other words, a turn towards the microburst center. Finally, a third type of extremals that can be found concerns trajectories featuring a turn to the left, or, in other words, a turn away from the microburst center. For a given value of the bank angle limit, the optimal angle-of-attack behavior is quite different for a left and a right turn, as can be observed from Fig. 9b, where results are shown for $\mu_{max} = 10°$. Also here the angle-of-attack behavior of the escape maneuver to the left results in an initial "zoom-climb", as can be seen in Fig. 9d.

Not surprisingly, escape maneuvers to the left, in which aircraft are turned away from the microburst center, lead to a much better performance. In fact, Fig. 9d makes clear that turning to the right even leads to a lower minimum altitude than not turning at all! Figure 9e shows the minimum altitude reached at any point along the trajectory as a function of the specified bank angle limit. Note that the curve shown in this figure is interrupted. The reason for this is that it proved to be impossible to compute escape trajectories that involve a turn to the right, but which pass the microburst center to the left. Note that the minimum altitude obtained for the unconstrained solution ($h_{min} = 42.3$m) is about 1.7m higher than for the lowest minimum altitude obtained for a constrained solution ($h_{min} = 40.6$m, for a right turn with $\mu_{max} = 10°$).

In addition to comparing the minimum altitudes achieved in turning and non-turning escape trajectories, we have also looked at alternative ways to express the performance improvements. For example, the minimum altitude achieved in a lateral escape maneuver to the left with $\mu_{max} = 10°$ is about 15m higher than the minimum altitude achieved in an escape maneuver with bank angle fixed at zero degrees. This corresponds to a reduction in the required advance warning time of about 2.4 seconds. This particular result has been obtained by delaying the initiation of the lateral escape maneuver while proceeding along the glideslope, such that the resulting minimum altitude is equal to the minimum altitude obtained for the non-turning trajectory. Alternatively, the lateral escape maneuver can be flown with an 8% increase in the windshear intensity and still achieve the same performance as the non-turning trajectory in this particular example.

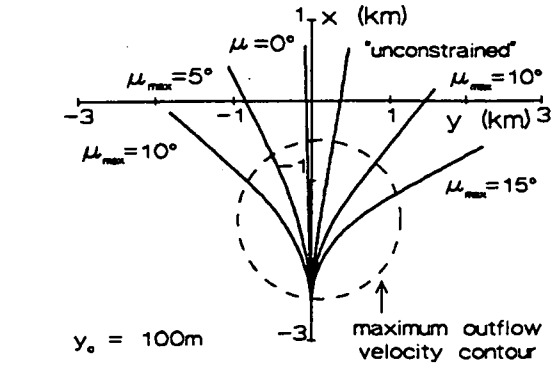

(a)

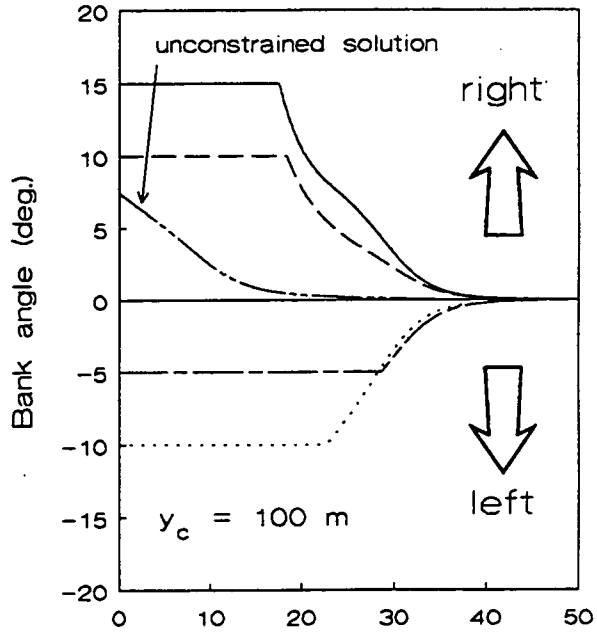

(c)

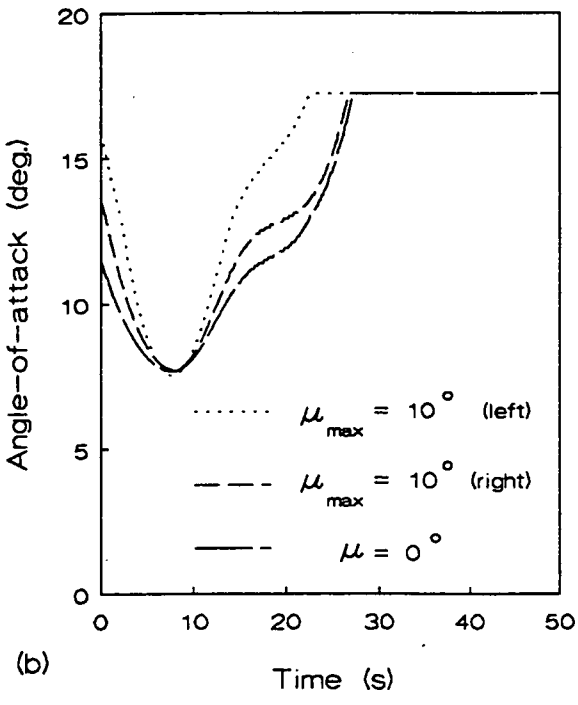

(b)

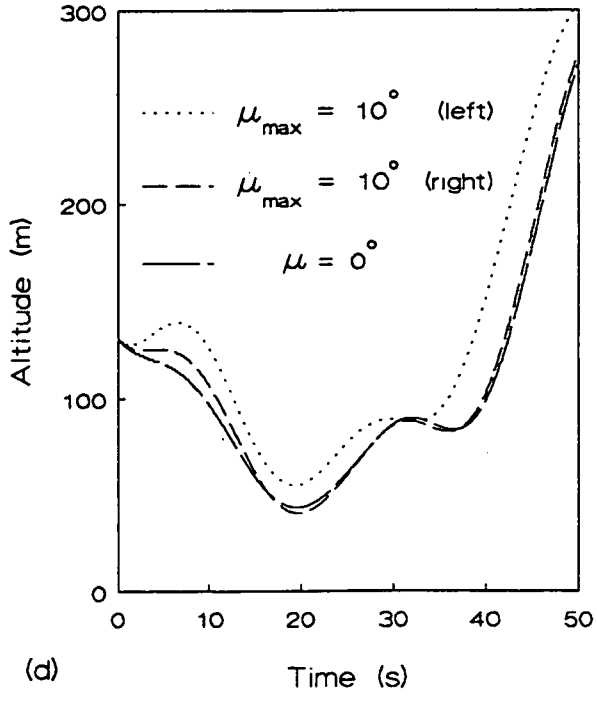

(d)

Figure 9 : Comparison of extremal solutions for various values of the bank angle limit. Distance of the microburst center to the runway threshold is 1500 m. The lateral displacement y_c is 100 m.

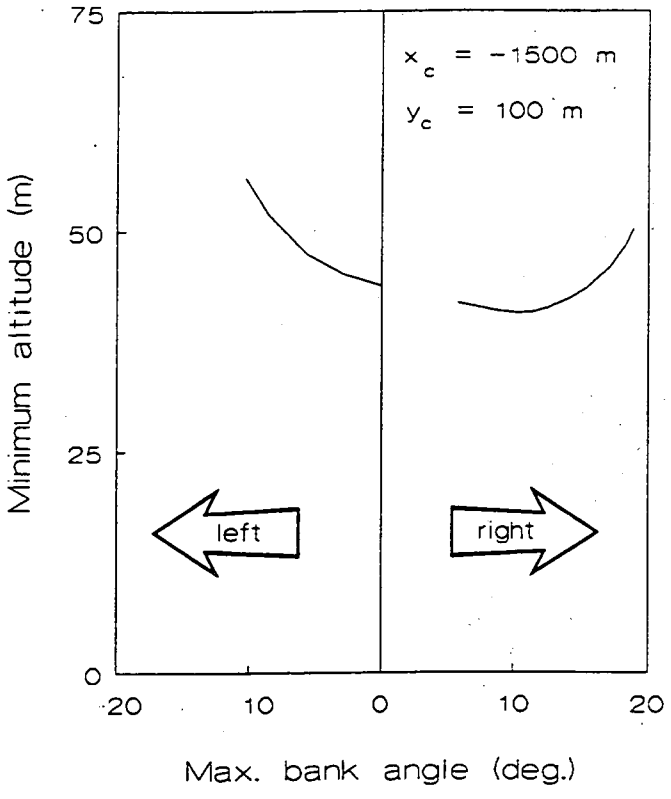

Figure 9 : (continued) Comparison of extremal solutions for various values of the bank angle limit. The distance of the microburst center to the runway threshold is 1500 m. The lateral displacement y_c is 100 m.

4.3 Effect of Displacing a Microburst Forward/Backward

This particular example serves to demonstrate the effect of displacing the center of the microburst forward/backward relative to the runway threshold. In this example the lateral microburst displacement y_c is set to -150 m, while all escape maneuvers are executed by making a right turn with $\mu_{max} = 10°$. The results are illustrated in the Figs. 10.

Fig. 10a shows the ground tracks of the three considered extremals. Note that one extremal starts well within the peak radial outflow velocity contour (x_c = -1750 m), whereas another starts well outside this contour (x_c = -1250 m).

Figures 10b and 10c show the control solutions. It is readily observed that the closer the microburst center is located to the threshold, the higher the initial angle-of-attack. Indeed, if the maneuver is initiated well outside the maximum radial outflow velocity contour, the aircraft can initially climb without experiencing a significant downdraft. Since in the presently employed model the vertical windspeed depends linearly on the altitude, climbing is clearly not advisable with in the downdraft region. This helps to explain the relatively large differences in altitude behavior that can be observed between the three extremals (Fig. 10d). Not surprisingly the differences in performance are also considerable.

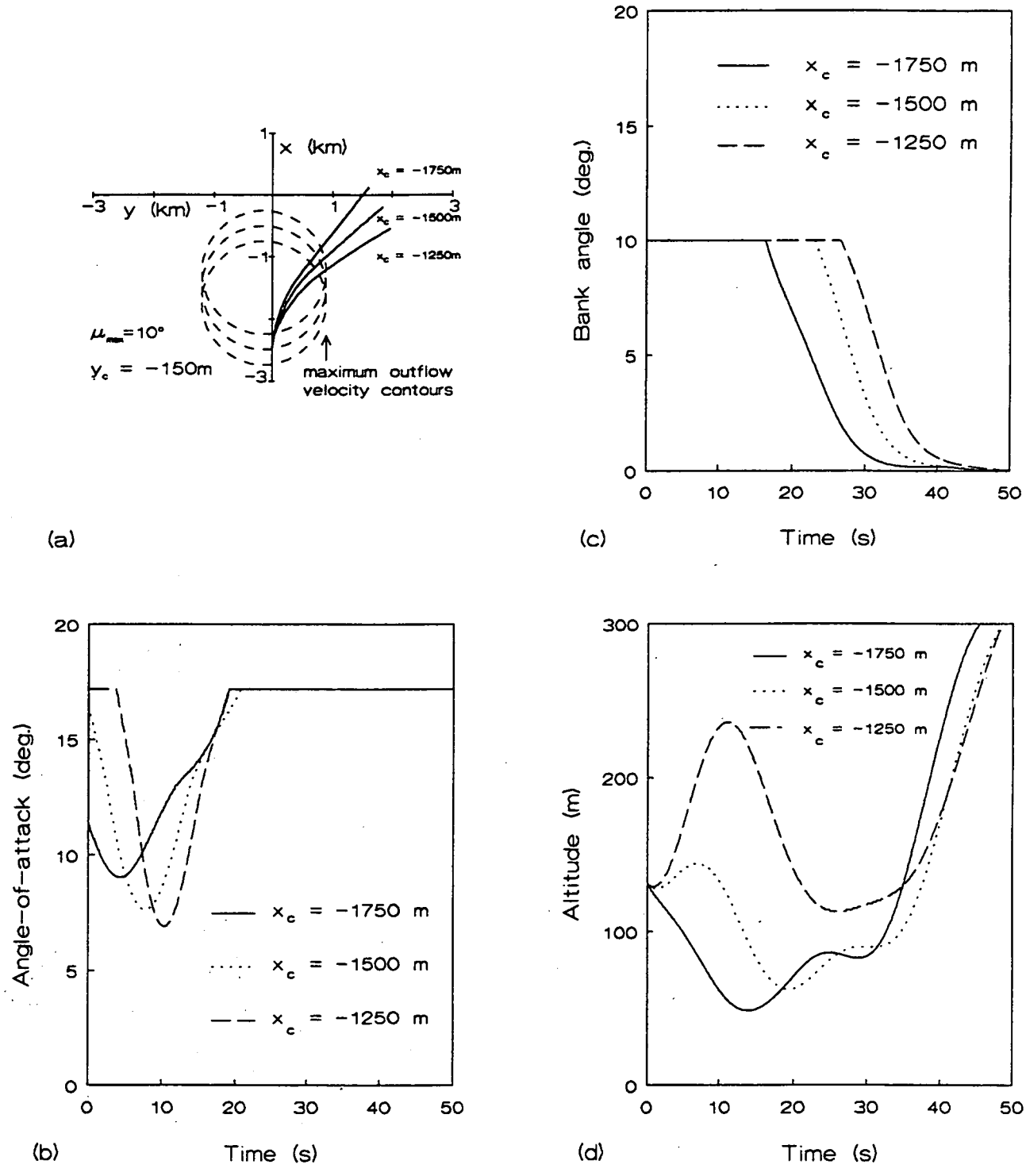

Figure 10 : Comparison of extremal solutions for various values of the distance of the microburst center to the runway threshold. The lateral displacement y_c is -150 m. The bank angle limit is 10°.

4.4 Influence of Initial Airspeed

The final example is intended to further illustrate the energy management features of lateral escape maneuvers. In this example the same geometry of the microburst encounter is considered as in the reference situation, but here the initial condition on airspeed has been varied. The results pertaining to three different values of initial airspeed are presented in the Figs. 11. Figure 11a shows that the lowest initial angle-of-attack is found for the extremal with the highest initial airspeed. However, Fig. 11b reveals that the overall influence of initial airspeed is such that a higher lift will be developed in the initial phase of the escape maneuver, when it is initiated with a higher airspeed. In other words, any increase in initial kinetic energy will be largely converted to potential energy such as to improve the turn rate in the initial phase.

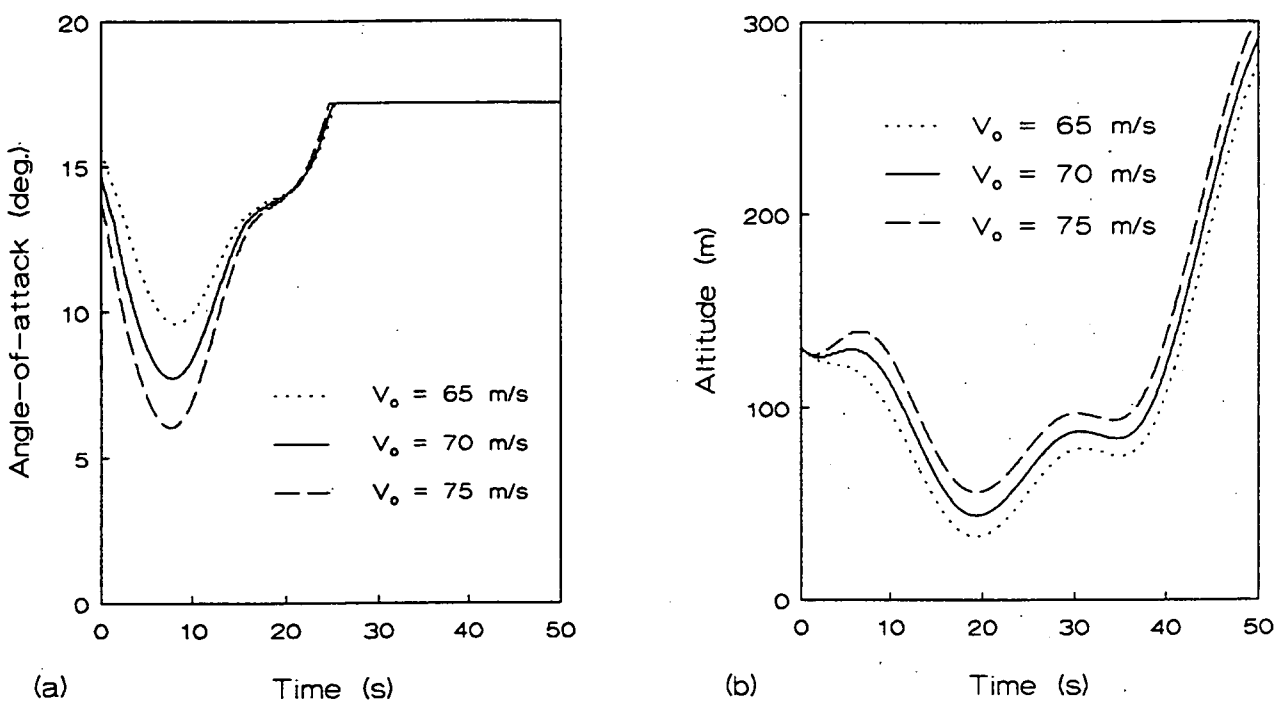

Figure 11 : Comparison of extremal solutions for various values of the initial airspeed. The distance of the microburst center to the runway threshold is 1500 m. There is no lateral displacement. The bank angle limit is 10°.

5. Guidance Solutions

In this Section a closed-loop guidance scheme is derived which approximates the open-loop optimal trajectories, relying on local (measurable) wind information only. With respect to the angle-of-attack, several guidance laws have been developed for near-optimal escape maneuvering in a vertical plane[4], which could have been used as a starting-point for the present analysis. However, in view of the findings of Ref.9, where advanced guidance laws were shown to offer little performance improvement in piloted simulation in comparison to a baseline constant pitch technique, it was decided to start out with the latter approach.

The simple constant pitch technique is used here in conjunction with a newly derived guidance law for the bank angle. From the behavior of the optimal trajectories (see, e.g., Figs. 8c and 8f) it was inferred that the guidance law for the bank angle should take the following simple form:

$$\mu = K(\chi_w - \chi) \quad , \quad |\mu| \leq \mu_{max} \quad , \tag{48}$$

with the gain coefficient K selected as 0.25 and where it is understood that:

$$-180° \leq \chi_w \leq 180° \quad , \quad -180° \leq \chi \leq 180° \tag{49}$$

The guidance law for the bank angle attempts to close the "heading error". This heading error being defined as the difference between the radial wind direction and the actual heading. The constant pitch guidance is based on a target pitch:

$$\alpha = \theta_{ref} - \gamma \quad , \quad 0 \leq \alpha \leq \alpha_{max} \quad , \tag{50}$$

with θ_{ref} selected as 15°. The feedback control scheme in Fig. 12 shows the implementation of the guidance laws. Clearly, the relatively modest (measured) information set needed, is not likely to pose a major stumbling block for the implementation of these guidance laws.

A substantial simulation effort has been undertaken to validate the proposed guidance laws. Analysis of the simulated feedback trajectories reveals a characteristic control behavior very similar to that of open-loop extremals (assuming these correspond to turning in the "correct" direction). For a particular case, namely, the reference situation with μ_{max} = 15°, the Figs. 13a and 13b show a comparison of the control behavior. Figure 13c shows the corresponding altitude behavior. Although there is clearly room for improvement, overall the proposed feedback strategy leads to a satisfactory performance. Moreover, unlike for the optimal trajectory computation, in the feedback trajectory simulations there are no numerical complications that prohibit specifying values for the bank angle limit larger than 15°. This is shown in Fig.8h, where a comparison of the minimum altitude as a function of the specified bank angle limit is made between feedback approximations and exact open-loop solutions (reference situation). It is clear

that in this particular case even further performance improvements can be expected, by allowing bank angles in excess of 30°. Especially for higher values of the specified bank angle limit, the simulated feedback results are remarkably close to the open-loop optimal results. In other words, the relatively simple constant pitch strategy which already proved to work quite well for escape maneuvers in a vertical plane, even performs better in lateral escape maneuvers. As a matter of fact, at this point it is felt that the guidance results are so good that they do not warrant any effort to develop more advanced pitch strategies, such as those developed by Miele et al. for flight in a vertical plane.

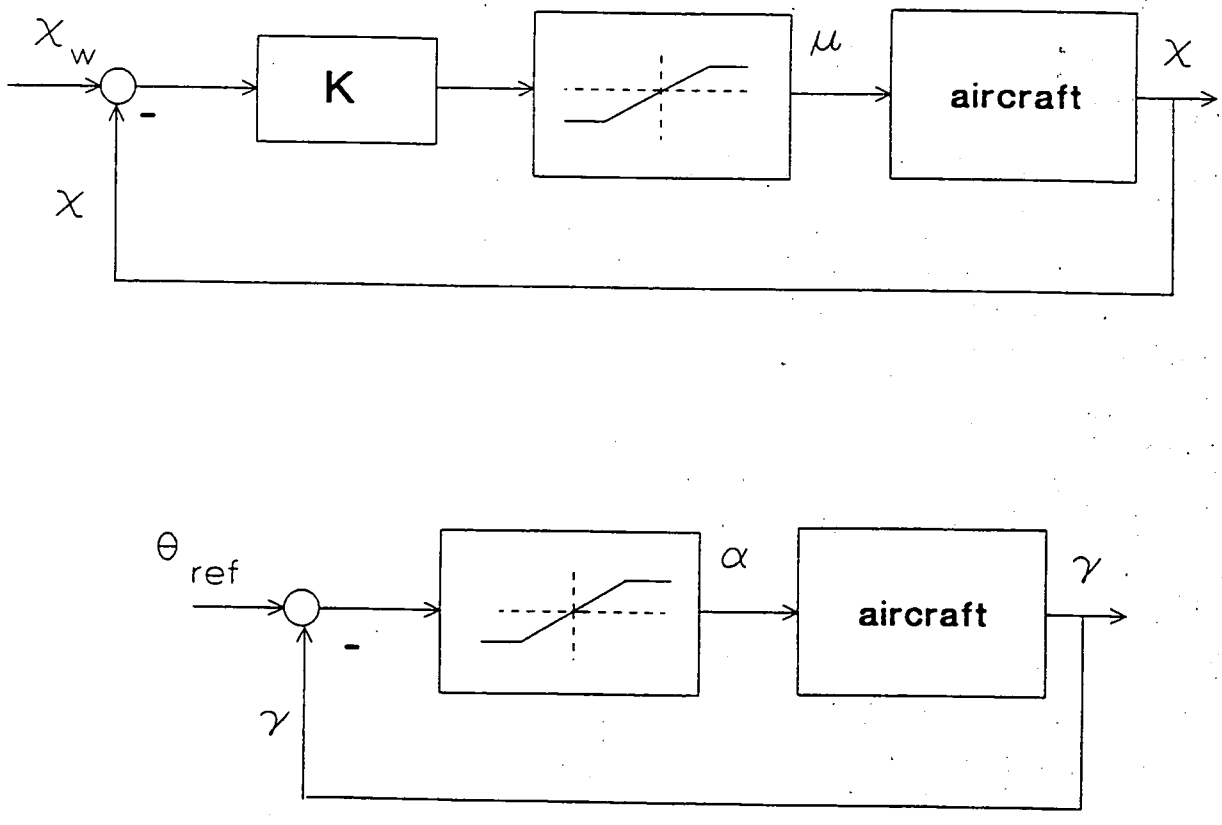

Figure 12 : Feedback guidance laws.

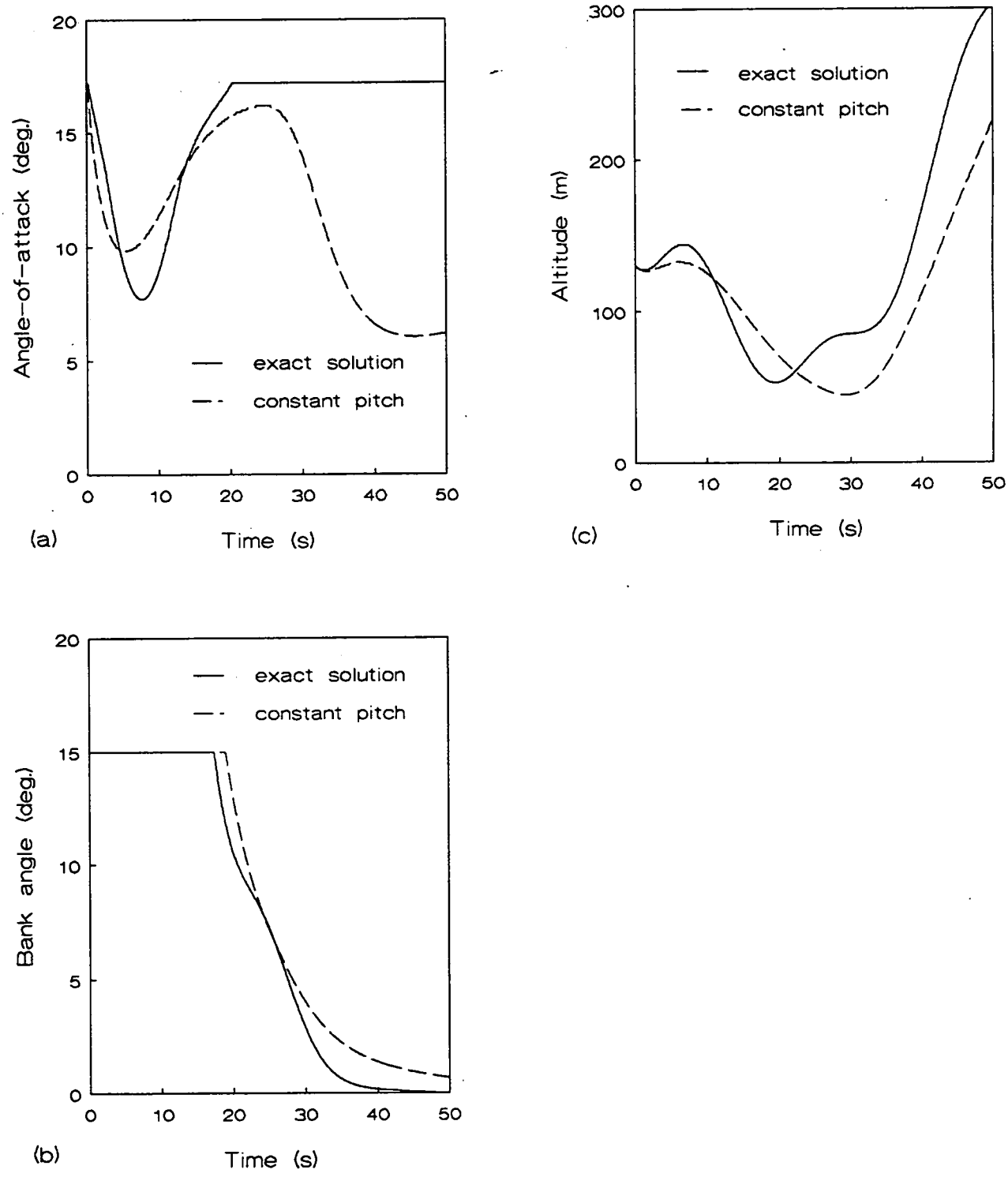

Figure 13 : Comparison between a simulated feedback solution and an exact open-loop optimal solution. The distance of the microburst center to the runway threshold is 1500 m. There is no lateral displacement. The bank angle limit is 15°.

6. Conclusions

Optimal lateral escape trajectories in a microburst wind field were studied for an aircraft on final approach. The performance index being minimized was the peak value of altitude drop. A simple, yet realistic, microburst model was used and different microburst locations were assumed. Full thrust was applied in all cases, so that only angle-of-attack and bank angle remained as control variables in the point-mass model.

Unfortunately, we have not been able to generate optimal lateral escape trajectories with a specified bank angle limit larger than 15°. However, for a specified value of the bank angle limit of that magnitude, typically three extremal solutions can be found, namely one trajectory passing the microburst center to the left, one trajectory passing the center to the right and one that passes right through the center. This behavior is found, regardless whether the microburst center is laterally displaced or not. Provided the aircraft turns away from the microburst center, lateral maneuvering leads to a significant improvement in the escape capability of the aircraft, even when the maneuver is initiated within the peak radial outflow velocity contour. On the other hand, in case of a flight with a lateral microburst displacement, incorrect lateral maneuvering may result in a performance loss.

It is clear that further research is required in order to obtain escape trajectories with a larger bank angle limit than currently possible. Some preliminary results indicate that the convergence-failure of the program can be possibly attributed to the currently employed performance index. Indeed, specifying higher values of h_{ref} in Eq.(27) has occasionally allowed the use of slightly higher bank angle limits. On the other hand, the use of larger values for h_{ref} was also shown to lead to considerably lower minimum altitudes. This raises the question how good the Bolza performance index of Eq.(27) (with the currently selected parameters) actually approximates the performance index of Eq.(26). Resorting to the alternative approach by converting the minimax problem into an equivalent optimal control problem with inequality constraints appears to have the potential to resolve these issues satisfactorily.

One of the most striking results established in this study relates to the energy management features of lateral maneuvering. In contrast to escape maneuvers that are restricted to the vertical plane, lateral escape maneuvers often exhibit an initial climb. It is believed that this climb results from the high initial lift which is needed to improve the turn rate. In other words, in an optimal lateral escape maneuver the best overall compromise between the conflicting requirements of a high initial turn rate (to take the aircraft away from the microburst center) and a low energy bleed-off rate (to maintain climb-gradient capability) is established.

A simple guidance scheme has been examined. Despite its simplicity, the guidance scheme produces a control behavior which closely resembles that of open-loop optimal solutions, in particular for higher values of the specified maximum bank angle. The required (measured) information set for this feedback law is rather modest, which should enable a relatively simple on-board implementation.

It has been recognized that model improvements need to be incorporated in future research. In particular, there is a need to make the response characteristics of the current control variables angle-of-attack and bank angle more realistic by including higher order dynamics in the model, i.e. by taking into account the time delay between the actual control inputs (control surface deflections) and the aircraft response.

It should be noted that the present investigations are essentially theoretical in nature and are primarily aimed at obtaining insight into the energy management features of

optimal lateral escape maneuvers. It is clear that a substantial research effort is still required before it is meaningful to address operational aspects.

References

1. Soesman, J.L, "Control of Aircraft Through Windshear During Final Approach", NLR Report TR 90117 L, 1990.
2. Miele, A., Wang, T. and Melvin, W.W., "Optimization and Acceleration Guidance of Flight Trajectories in a Windshear", *Journal of Guidance, Control, and Dynamics*, Vol.10, July-August 1987, pp. 368-377.
3. Miele, A., Wang, T. and Melvin, W.W., "Penetration Landing Guidance Trajectories in the Presence of Windshear", *Journal of Guidance, Control, and Dynamics*, Vol.12, Nov.-Dec. 1989, pp. 806-814.
4. Miele, A., Wang, T., Melvin, W.W. and Bowles, R.L., "Acceleration, Gamma and Theta Guidance for Abort Landing in a Windshear", *Journal of Guidance, Control, and Dynamics*, Vol.12, Nov.-Dec. 1989, pp. 815-821.
5. Zhao,Y. and Bryson, A.E., "Optimal Paths Through Downbursts", *Journal of Guidance, Control, and Dynamics*, Vol.13, Sept.-Oct. 1990, pp. 813-818.
6. Zhao,Y. and Bryson, A.E., "Control of an Aircraft in Downbursts", *Journal of Guidance, Control, and Dynamics*, Vol.13, Sept.-Oct. 1990, pp. 819-823.
7. Psiaki, M.L. and Stengel, R.F., "Optimal Flight Paths Through Microburst Wind Profiles", *Journal of Aircraft*, Vol.23, August 1986, pp. 629-635.
8. Psiaki, M.L. and Stengel, R.F., "Optimal Aircraft Performance During Microburst Encounter", *Journal of Guidance, Control, and Dynamics*, Vol.14, March-April 1991, pp. 440-446.
9. Hinton, D.A. "Forward-Look Wind-Shear Detection for Microburst Recovery", *Journal of Aircraft*, Vol.29, Jan.-Feb. 1992, pp. 63-66.
10. Bowles, R.L., Reducing Windshear Risk Through Airborne Systems Technology, Proceedings of the 17th ICAS, Stockholm, 1990, pp. 1603-1630.
11. Avila de Melo, D. and Hansman, R.J., "Analysis of Aircraft Performance During Lateral Maneuvering for Microburst Avoidance", *Journal of Aircraft*, Vol.28, Dec. 1991, pp. 837-842.
12. Federal Aviation Administration Windshear Training Aid, U.S. Dept. of Transportation, Associate Administration for Development and Logistics, Washington DC, 1987.
13. Bryson, A.E. and Ho, Y.-C., "Applied Optimal Control", Hemisphere Publishing Corporation, Washington, 1975.
14. Grimm, W., Berger, E. and Oberle, H.J., "Benutzeranleitung fur das Rechenprogram BNDSCO zur Lösung Beschrankter Optimaler Steuerungsprobleme", DFVLR-Mitt. 85-05, 1984.
15. Bulirsch, R. Montrone, F. and Pesch, H.J., "Abort Landing in the Presence of Windshear as a Minimax Optimal Control Problem, Part 1: Necessary Conditions," *Journal of Optimization Theory and Applications*, Vol. 70, July 1991, pp. 1-23.15.
16. Bulirsch, R. Montrone, F. and Pesch, H.J., "Abort Landing in the Presence of Windshear as a Minimax Optimal Control Problem, Part 2: Multiple Shooting and Homotopy," *Journal of Optimization Theory and Applications*, Vol. 70, Aug. 1991, pp. 223-254.

Appendix A : Evaluation of some Partial Derivatives

A.1 Partial Derivatives of the Hamiltonian with Respect to the State Variables

The following presents an overview of the right-hand sides of the adjoint equations (29) through (35):

$$
\begin{aligned}
\frac{\partial H}{\partial x} &= \lambda_x \frac{\partial W_x}{\partial x} + \lambda_y \frac{\partial W_y}{\partial x} + \lambda_h \frac{\partial W_h}{\partial x} + \lambda_E \{ \frac{\partial W_h}{\partial x} \\
&- \frac{V \cos\gamma \cos\chi}{g} [\frac{\partial^2 W_x}{\partial x^2} \dot{x} + (\frac{\partial W_x}{\partial x})^2 + \frac{\partial^2 W_x}{\partial x \partial y} \dot{y} + \frac{\partial W_x}{\partial y} \frac{\partial W_y}{\partial x}] \\
&- \frac{V \cos\gamma \sin\chi}{g} [\frac{\partial^2 W_y}{\partial x^2} \dot{x} + \frac{\partial W_y}{\partial x} \frac{\partial W_x}{\partial x} + \frac{\partial^2 W_y}{\partial x \partial y} \dot{y} + \frac{\partial W_y}{\partial y} \frac{\partial W_y}{\partial x}] \\
&- \frac{V \sin\gamma}{g} [\frac{\partial^2 W_h}{\partial x^2} \dot{x} + \frac{\partial W_h}{\partial x} \frac{\partial W_x}{\partial x} + \frac{\partial^2 W_h}{\partial x \partial y} \dot{y} + \frac{\partial W_h}{\partial y} \frac{\partial W_y}{\partial x} \\
&+ \frac{\partial^2 W_h}{\partial x \partial h} \dot{h} + \frac{\partial W_h}{\partial h} \frac{\partial W_h}{\partial x}] \} \\
&+ \lambda_\gamma \{ \frac{\sin\gamma \cos\chi}{V} [\frac{\partial^2 W_x}{\partial x^2} \dot{x} + (\frac{\partial W_x}{\partial x})^2 + \frac{\partial^2 W_x}{\partial x \partial y} \dot{y} + \frac{\partial W_x}{\partial y} \frac{\partial W_y}{\partial x}] \\
&+ \frac{\sin\gamma \sin\chi}{V} [\frac{\partial^2 W_y}{\partial x^2} \dot{x} + \frac{\partial W_y}{\partial x} \frac{\partial W_x}{\partial x} + \frac{\partial^2 W_y}{\partial x \partial y} \dot{y} + \frac{\partial W_y}{\partial y} \frac{\partial W_y}{\partial x}] \\
&- \frac{\cos\gamma}{V} [\frac{\partial^2 W_h}{\partial x^2} \dot{x} + \frac{\partial W_h}{\partial x} \frac{\partial W_x}{\partial x} + \frac{\partial^2 W_h}{\partial x \partial y} \dot{y} + \frac{\partial W_h}{\partial y} \frac{\partial W_y}{\partial x} \\
&+ \frac{\partial^2 W_h}{\partial x \partial h} \dot{h} + \frac{\partial W_h}{\partial h} \frac{\partial W_h}{\partial x}] \} \\
&+ \lambda_\chi \{ \frac{\sin\chi}{V \cos\gamma} [\frac{\partial^2 W_x}{\partial x^2} \dot{x} + (\frac{\partial W_x}{\partial x})^2 + \frac{\partial^2 W_x}{\partial x \partial y} \dot{y} + \frac{\partial W_x}{\partial y} \frac{\partial W_y}{\partial x}] \\
&- \frac{\cos\chi}{V \cos\gamma} [\frac{\partial^2 W_y}{\partial x^2} \dot{x} + \frac{\partial W_y}{\partial x} \frac{\partial W_x}{\partial x} + \frac{\partial^2 W_y}{\partial x \partial y} \dot{y} + \frac{\partial W_y}{\partial y} \frac{\partial W_y}{\partial x}] \}
\end{aligned}
\tag{51}
$$

$$
\begin{aligned}
\frac{\partial H}{\partial y} &= \lambda_x \frac{\partial W_x}{\partial y} + \lambda_y \frac{\partial W_y}{\partial y} + \lambda_h \frac{\partial W_h}{\partial y} + \lambda_E \{ \frac{\partial W_h}{\partial y} \\
&- \frac{V \cos\gamma \cos\chi}{g} [\frac{\partial^2 W_x}{\partial x \partial y} \dot{x} + \frac{\partial W_x}{\partial x} \frac{\partial W_x}{\partial y} + \frac{\partial^2 W_x}{\partial y^2} \dot{y} + \frac{\partial W_x}{\partial y} \frac{\partial W_y}{\partial y}] \\
&- \frac{V \cos\gamma \sin\chi}{g} [\frac{\partial^2 W_y}{\partial x \partial y} \dot{x} + \frac{\partial W_y}{\partial x} \frac{\partial W_x}{\partial y} + \frac{\partial^2 W_y}{\partial y^2} \dot{y} + (\frac{\partial W_y}{\partial y})^2] \\
&- \frac{V \sin\gamma}{g} [\frac{\partial^2 W_h}{\partial x \partial y} \dot{x} + \frac{\partial W_h}{\partial x} \frac{\partial W_x}{\partial y} + \frac{\partial^2 W_h}{\partial y^2} \dot{y} + \frac{\partial W_h}{\partial y} \frac{\partial W_y}{\partial y} \\
&+ \frac{\partial^2 W_h}{\partial y \partial h} \dot{h} + \frac{\partial W_h}{\partial h} \frac{\partial W_h}{\partial y}] \} \\
&+ \lambda_\gamma \{ \frac{\sin\gamma \cos\chi}{V} [\frac{\partial^2 W_x}{\partial x \partial y} \dot{x} + \frac{\partial W_x}{\partial x} \frac{\partial W_x}{\partial y} + \frac{\partial^2 W_x}{\partial y^2} \dot{y} + \frac{\partial W_x}{\partial y} \frac{\partial W_y}{\partial y}] \\
&+ \frac{\sin\gamma \sin\chi}{V} [\frac{\partial^2 W_y}{\partial x \partial y} \dot{x} + \frac{\partial W_y}{\partial x} \frac{\partial W_x}{\partial y} + \frac{\partial^2 W_y}{\partial y^2} \dot{y} + (\frac{\partial W_y}{\partial y})^2] \\
&- \frac{\cos\gamma}{V} [\frac{\partial^2 W_h}{\partial x \partial y} \dot{x} + \frac{\partial W_h}{\partial x} \frac{\partial W_x}{\partial y} + \frac{\partial^2 W_h}{\partial y^2} \dot{y} + \frac{\partial W_h}{\partial y} \frac{\partial W_y}{\partial y} \\
&+ \frac{\partial^2 W_h}{\partial y \partial h} \dot{h} + \frac{\partial W_h}{\partial h} \frac{\partial W_h}{\partial y}] \} \\
&+ \lambda_\chi \{ \frac{\sin\chi}{V \cos\gamma} [\frac{\partial^2 W_x}{\partial x \partial y} \dot{x} + \frac{\partial W_x}{\partial x} \frac{\partial W_x}{\partial y} + \frac{\partial^2 W_x}{\partial y^2} \dot{y} + \frac{\partial W_x}{\partial y} \frac{\partial W_y}{\partial y}] \\
&- \frac{\cos\chi}{V \cos\gamma} [\frac{\partial^2 W_y}{\partial x \partial y} \dot{x} + \frac{\partial W_y}{\partial x} \frac{\partial W_x}{\partial y} + \frac{\partial^2 W_y}{\partial y^2} \dot{y} + (\frac{\partial W_y}{\partial y})^2] \}
\end{aligned}
\tag{52}
$$

$$\frac{\partial H}{\partial h}|V = n(h_{ref}-h)^n + \lambda_h\frac{\partial W_h}{\partial h} + \lambda_E\{\frac{V}{W}(\frac{\partial T}{\partial h} - \frac{\partial D}{\partial h}) + \frac{\partial W_h}{\partial h}$$
$$- \frac{V}{g}\sin\gamma[\frac{\partial^2 W_h}{\partial h\partial x}\dot{x} + \frac{\partial^2 W_h}{\partial h\partial y}\dot{y} + (\frac{\partial W_h}{\partial h})^2]\}$$
$$+ \lambda_\gamma\{\frac{g}{V}\frac{\partial L}{\partial h}\frac{\cos\mu}{W} - \frac{\cos\gamma}{V}[\frac{\partial^2 W_h}{\partial h\partial x}\dot{x} + \frac{\partial^2 W_h}{\partial h\partial y}\dot{y} + (\frac{\partial W_h}{\partial h})^2]\} \quad (53)$$
$$+ \lambda_\chi\{\frac{g}{V\cos\gamma}\frac{\partial L}{\partial h}\frac{\sin\mu}{W}\}$$

$$\frac{\partial H}{\partial V}|h = \lambda_x\cos\gamma\cos\chi + \lambda_y\cos\gamma\sin\chi + \lambda_h\sin\gamma$$
$$+ \lambda_E\{\frac{(T-D)}{W} + \frac{V}{W}(\frac{\partial T}{\partial V} - \frac{\partial D}{\partial V})$$
$$- \frac{\cos\gamma\cos\chi}{g}[\frac{\partial W_x}{\partial x}(2V\cos\gamma\cos\chi + W_x) + \frac{\partial W_x}{\partial y}(2V\cos\gamma\sin\chi + W_y)]$$
$$- \frac{\cos\gamma\sin\chi}{g}[\frac{\partial W_y}{\partial x}(2V\cos\gamma\cos\chi + W_x) + \frac{\partial W_y}{\partial y}(2V\cos\gamma\sin\chi + W_y)]$$
$$- \frac{\sin\gamma}{g}[\frac{\partial W_h}{\partial x}(2V\cos\gamma\cos\chi + W_x) + \frac{\partial W_h}{\partial y}(2V\cos\gamma\sin\chi + W_y) \quad (54)$$
$$+ \frac{\partial W_h}{\partial h}(2V\sin\gamma + W_h)]\} + \lambda_\gamma\{\frac{g}{V^2}[\frac{L\cos\mu}{W} + \cos\gamma]$$
$$- \frac{\sin\gamma\cos\chi}{V^2}[\frac{\partial W_x}{\partial x}W_x + \frac{\partial W_x}{\partial y}W_y] - \frac{\sin\gamma\sin\chi}{V^2}[\frac{\partial W_y}{\partial x}W_x + \frac{\partial W_y}{\partial y}W_y]$$
$$+ \frac{\cos\gamma}{V^2}[\frac{\partial W_h}{\partial x}W_x + \frac{\partial W_h}{\partial y}W_y + \frac{\partial W_h}{\partial h}W_h]\} + \lambda_\chi\{[\frac{g}{V^2\cos\gamma}\frac{L\sin\mu}{W}]$$
$$- \frac{\sin\chi}{V^2\cos\gamma}[\frac{\partial W_x}{\partial x}W_x + \frac{\partial W_x}{\partial y}W_y] + \frac{\cos\chi}{V^2\cos\gamma}[\frac{\partial W_y}{\partial x}W_x + \frac{\partial W_y}{\partial y}W_y]\}$$

$$
\begin{aligned}
\frac{\partial H}{\partial \gamma} &= -\lambda_x V\sin\gamma\cos\chi - \lambda_y V\sin\gamma\sin\chi + \lambda_h V\cos\gamma \\
&+ \lambda_E\{\frac{V\sin\gamma\cos\chi}{g}[\frac{\partial W_x}{\partial x}(2V\cos\gamma\cos\chi + W_x) + \frac{\partial W_x}{\partial y}(2V\cos\gamma\sin\chi + W_y)] \\
&+ \frac{V\sin\gamma\sin\chi}{g}[\frac{\partial W_y}{\partial x}(2V\cos\gamma\cos\chi + W_x) + \frac{\partial W_y}{\partial y}(2V\cos\gamma\sin\chi + W_y)] \\
&- \frac{V}{g}\frac{\partial W_h}{\partial x}[V\cos\chi(\cos^2\gamma - \sin^2\gamma) + W_x\cos\gamma] \\
&- \frac{V}{g}\frac{\partial W_h}{\partial y}[V\sin\chi(\cos^2\gamma - \sin^2\gamma) + W_y\cos\gamma] \\
&- \frac{V\cos\gamma}{g}\frac{\partial W_h}{\partial h}(2V\sin\gamma + W_h)\} + \lambda_\gamma\{\frac{g}{V}\sin\gamma \\
&+ \frac{\cos\chi}{V}\frac{\partial W_x}{\partial x}[V\cos\chi(\cos^2\gamma - \sin^2\gamma) + W_x\cos\gamma] \\
&+ \frac{\cos\chi}{V}\frac{\partial W_x}{\partial y}[V\sin\chi(\cos^2\gamma - \sin^2\gamma) + W_y\cos\gamma] \\
&+ \frac{\sin\chi}{V}\frac{\partial W_y}{\partial x}[V\cos\chi(\cos^2\gamma - \sin^2\gamma) + W_x\cos\gamma] \\
&+ \frac{\sin\chi}{V}\frac{\partial W_y}{\partial y}[V\sin\chi(\cos^2\gamma - \sin^2\gamma) + W_y\cos\gamma] \\
&+ \frac{\sin\gamma}{V}\frac{\partial W_h}{\partial x}[(2V\cos\gamma\cos\chi + W_x) + \frac{\partial W_h}{\partial y}(2V\cos\gamma\sin\chi + W_y)] \\
&+ \frac{1}{V}\frac{\partial W_h}{\partial h}[V(\sin^2\gamma - \cos^2\gamma) + W_h\sin\gamma]\} \\
&+ \lambda_\chi\{[\frac{g\sin\gamma}{V\cos^2\gamma}\frac{L\sin\mu}{W}] \\
&+ \frac{\sin\gamma}{V\cos^2\gamma}[(\frac{\partial W_x}{\partial x}W_x + \frac{\partial W_x}{\partial y}W_y)\sin\chi - (\frac{\partial W_y}{\partial x}W_x + \frac{\partial W_y}{\partial y}W_y)\cos\chi]\}
\end{aligned}
\tag{55}
$$

$$\frac{\partial H}{\partial \chi} = -\lambda_x V\cos\gamma\sin\chi + \lambda_y V\cos\gamma\cos\chi$$
$$+ \lambda_E\{\frac{V\cos\gamma\sin\chi}{g}\frac{\partial W_x}{\partial x}(2V\cos\gamma\cos\chi + W_x)$$
$$- \frac{V\cos\gamma}{g}\frac{\partial W_x}{\partial y}[V\cos\chi(\cos^2\gamma - \sin^2\gamma) - W_y\sin\chi]$$
$$- \frac{V\cos\gamma}{g}[\frac{\partial W_y}{\partial x}[V\cos\chi(\cos^2\gamma - \sin^2\gamma) + W_x\cos\chi]$$
$$- \frac{V\cos\gamma\cos\chi}{g}\frac{\partial W_y}{\partial y}(2V\cos\gamma\sin\chi + W_y)$$
$$+ \frac{V^2\cos\gamma\sin\gamma}{g}(\frac{\partial W_h}{\partial x}\sin\chi - \frac{\partial W_h}{\partial y}\cos\chi)\}$$
$$+ \lambda_\gamma\{ - \frac{\sin\gamma\sin\chi}{V}\frac{\partial W_x}{\partial x}(2V\cos\gamma\cos\chi + W_x)$$
$$+ \frac{\sin\gamma}{V}\frac{\partial W_x}{\partial y}[V\cos\gamma(\cos^2\chi - \sin^2\chi) - W_y\sin\chi] \qquad (56)$$
$$+ \frac{\sin\gamma}{V}\frac{\partial W_y}{\partial x}[V\cos\gamma(\cos^2\chi - \sin^2\chi) + W_x\cos\chi]$$
$$+ \frac{\sin\gamma\cos\chi}{V}\frac{\partial W_y}{\partial y}(2V\cos\gamma\sin\chi + W_y)$$
$$+ \cos^2\gamma(\frac{\partial W_h}{\partial x}\sin\chi - \frac{\partial W_h}{\partial y}\cos\chi)\}$$
$$+ \lambda_\chi\{\frac{1}{V\cos\gamma}\frac{\partial W_x}{\partial x}[V\cos\gamma(\cos^2\chi - \sin^2\chi) + W_x\cos\chi]$$
$$+ \frac{\cos\chi}{V\cos\gamma}\frac{\partial W_x}{\partial y}(2V\cos\gamma\sin\chi + W_y)$$
$$+ \frac{\sin\chi}{V\cos\gamma}\frac{\partial W_y}{\partial x}(2V\cos\gamma\cos\chi + W_x)$$
$$- \frac{1}{V\cos\gamma}\frac{\partial W_y}{\partial y}[V\cos\gamma(\cos^2\chi - \sin^2\chi) - W_y\sin\chi]\}$$

$$\frac{\partial H}{\partial \beta} = \lambda_E\frac{\partial T}{\partial \beta}\frac{V}{W} - \lambda_\beta\frac{1}{\tau} \qquad (57)$$

A.2 Partial Derivatives of Thrust, Lift and Drag with Respect to the State Variables

The thrust, lift and drag functions are defined in the Eqs.(12) through (15). The following partial derivatives of thrust, lift and drag arise in the equations (51) through (57):

$$\frac{\partial T}{\partial \beta} = T_{max} \quad ; \quad \frac{\partial T}{\partial V} = \beta[T_1 + 2T_2 V] \tag{58}$$

$$\frac{\partial L}{\partial h} = \frac{L}{\rho}\frac{\partial \rho}{\partial h} \tag{59}$$

$$\frac{\partial D}{\partial h} = \frac{D}{\rho}\frac{\partial \rho}{\partial h} \quad ; \quad \frac{\partial D}{\partial V} = 2\frac{D}{V} \tag{60}$$

A.3 Partial Derivatives of the Windvelocity Vector

Let us define:

$$\Delta x \triangleq x - x_c \quad ; \quad \Delta y \triangleq y - y_c \tag{61}$$

Using these definitions it is clear that Eq.(20) can be expressed as:

$$r = \sqrt{\Delta x^2 + \Delta y^2} \tag{62}$$

The horizontal wind direction χ_w at a given spatial location is given by (see Fig. 4):

$$\chi_w = \arccos(\Delta x / r) \cdot sign(\Delta y)$$

The following partial derivatives of r with respect to x, y and h are needed:

$$\frac{\partial r}{\partial x} = \frac{\Delta x}{r} = \cos\chi_w \quad , \quad \frac{\partial r}{\partial y} = \frac{\Delta y}{r} = \sin\chi_w \tag{64}$$

$$\frac{\partial^2 r}{\partial x^2} = \frac{(\Delta y)^2}{r^3} \quad , \quad \frac{\partial^2 r}{\partial y^2} = \frac{(\Delta x)^2}{r^3} \quad , \quad \frac{\partial^2 r}{\partial x \partial y} = -\frac{\Delta x \Delta y}{r^3} \tag{65}$$

$$\frac{\partial^3 r}{\partial x^3} = -\frac{3(\Delta y)^2 \Delta x}{r^5} \quad , \quad \frac{\partial^3 r}{\partial y^3} = -\frac{3\Delta y (\Delta x)^2}{r^5} \tag{66}$$

$$\frac{\partial^3 r}{\partial x^2 \partial y} = \frac{\Delta y[2r^2 - 3(\Delta y)^2]}{r^5} \quad , \quad \frac{\partial^3 r}{\partial x \partial y^2} = \frac{\Delta x[2r^2 - 3(\Delta x)^2]}{r^5} \tag{67}$$

Using Eq.(18), the required partial derivatives of the radial windspeed W_r with respect to the radial distance r can be calculated as:

$$\frac{\partial W_r}{\partial r} = f_r \left(\frac{-(\frac{r - D/2}{200})}{[(\frac{r - D/2}{200})^2 + 10]^2} + \frac{(\frac{r + D/2}{200})}{[(\frac{r + D/2}{200})^2 + 10]^2} \right) \tag{68}$$

$$\frac{\partial^2 W_r}{\partial r^2} = f_r \left(\frac{0.02\,(\frac{r - D/2}{200})^2}{[(\frac{r - D/2}{200})^2 + 10]^3} - \frac{0.005}{[(\frac{r - D/2}{200})^2 + 10]^2} - \frac{0.02\,(\frac{r + D/2}{200})^2}{[(\frac{r + D/2}{200})^2 + 10]^3} + \frac{0.005}{[(\frac{r + D/2}{200})^2 + 10]^2} \right) \tag{69}$$

With the above information available and making use of Eq.(21), it is now possible to calculate the partial derivatives of the radial wind velocity W_r with respect to the position coordinates x and y:

$$\frac{\partial W_r}{\partial x} = \frac{\partial W_r}{\partial r}\frac{\partial r}{\partial x} \quad , \quad \frac{\partial W_r}{\partial y} = \frac{\partial W_r}{\partial r}\frac{\partial r}{\partial y} \tag{70}$$

$$\frac{\partial^2 W_r}{\partial x^2} = \frac{\partial^2 W_r}{\partial r^2}\left(\frac{\partial r}{\partial x}\right)^2 + \frac{\partial W_r}{\partial r}\frac{\partial^2 r}{\partial x^2} \tag{71}$$

$$\frac{\partial^2 W_r}{\partial y^2} = \frac{\partial^2 W_r}{\partial r^2}\left(\frac{\partial r}{\partial y}\right)^2 + \frac{\partial W_r}{\partial r}\frac{\partial^2 r}{\partial y^2} \tag{72}$$

$$\frac{\partial^2 W_r}{\partial x \partial y} = \frac{\partial^2 W_r}{\partial r^2}\frac{\partial r}{\partial x}\frac{\partial r}{\partial y} + \frac{\partial W_r}{\partial r}\frac{\partial^2 r}{\partial x \partial y} \tag{73}$$

Finally the partial derivatives of the horizontal wind components W_x and W_y are computed:

$$\frac{\partial W_x}{\partial x} = \frac{\partial W_r}{\partial x}\frac{\partial r}{\partial x} + W_r\frac{\partial^2 r}{\partial x^2} \tag{74}$$

$$\frac{\partial W_x}{\partial y} = \frac{\partial W_r}{\partial y}\frac{\partial r}{\partial x} + W_r\frac{\partial^2 r}{\partial x \partial y} \tag{75}$$

$$\frac{\partial^2 W_x}{\partial x^2} = \frac{\partial^2 W_r}{\partial x^2}\frac{\partial r}{\partial x} + 2\frac{\partial W_r}{\partial x}\frac{\partial^2 r}{\partial x^2} + W_r\frac{\partial^3 r}{\partial x^3} \tag{76}$$

$$\frac{\partial^2 W_x}{\partial y^2} = \frac{\partial^2 W_r}{\partial y^2}\frac{\partial r}{\partial x} + 2\frac{\partial W_r}{\partial y}\frac{\partial^2 r}{\partial x \partial y} + W_r\frac{\partial^3 r}{\partial x \partial y^2} \tag{77}$$

$$\frac{\partial^2 W_x}{\partial x \partial y} = \frac{\partial^2 W_r}{\partial x \partial y}\frac{\partial r}{\partial x} + \frac{\partial W_r}{\partial y}\frac{\partial^2 r}{\partial x^2} + \frac{\partial W_r}{\partial x}\frac{\partial^2 r}{\partial x \partial y} + W_r\frac{\partial^3 r}{\partial x^2 \partial y} \tag{78}$$

$$\frac{\partial W_y}{\partial x} = \frac{\partial W_r}{\partial x}\frac{\partial r}{\partial y} + W_r\frac{\partial^2 r}{\partial x \partial y} \tag{79}$$

$$\frac{\partial W_y}{\partial y} = \frac{\partial W_r}{\partial y}\frac{\partial r}{\partial y} + W_r\frac{\partial^2 r}{\partial y^2} \tag{80}$$

$$\frac{\partial^2 W_y}{\partial x^2} = \frac{\partial^2 W_r}{\partial x^2}\frac{\partial r}{\partial y} + 2\frac{\partial W_r}{\partial x}\frac{\partial^2 r}{\partial x \partial y} + W_r\frac{\partial^3 r}{\partial x^2 \partial y} \tag{81}$$

$$\frac{\partial^2 W_y}{\partial y^2} = \frac{\partial^2 W_r}{\partial y^2}\frac{\partial r}{\partial y} + 2\frac{\partial W_r}{\partial y}\frac{\partial^2 r}{\partial y^2} + W_r\frac{\partial^3 r}{\partial y^3} \tag{82}$$

$$\frac{\partial^2 W_y}{\partial x \partial y} = \frac{\partial^2 W_r}{\partial x \partial y}\frac{\partial r}{\partial y} + \frac{\partial W_r}{\partial x}\frac{\partial^2 r}{\partial y^2} + \frac{\partial W_r}{\partial y}\frac{\partial^2 r}{\partial x \partial y} + W_r\frac{\partial^3 r}{\partial x \partial y^2} \tag{83}$$

In an entire similar fashion, the required partials of the vertical windspeed W_h can be evaluated using Eq.(19) and the above relations:

$$\frac{\partial W_h}{\partial r} = f_h\left(\frac{0.004\,h\,(\frac{r}{400})^3}{[(\frac{r}{400})^4 + 10]^2}\right) \tag{84}$$

$$\frac{\partial^2 W_h}{\partial r^2} = f_h\left(\frac{-0.00008\,h\,(\frac{r}{400})^6}{[(\frac{r}{400})^4 + 10]^3} + \frac{0.00003\,h\,(\frac{r}{400})^2}{[(\frac{r}{400})^4 + 10]^2}\right) \tag{85}$$

$$\frac{\partial W_h}{\partial h} = \frac{W_h}{h}\ , \quad \frac{\partial^2 W_h}{\partial r \partial h} = \frac{1}{h}\frac{\partial W_h}{\partial r} \tag{86}$$

$$\frac{\partial W_h}{\partial x} = \frac{\partial W_h}{\partial r}\frac{\partial r}{\partial x}\ , \quad \frac{\partial W_h}{\partial y} = \frac{\partial W_h}{\partial r}\frac{\partial r}{\partial y} \tag{87}$$

$$\frac{\partial^2 W_h}{\partial x^2} = \frac{\partial^2 W_h}{\partial r^2}(\frac{\partial r}{\partial x})^2 + \frac{\partial W_h}{\partial r}\frac{\partial^2 r}{\partial x^2}\ , \quad \frac{\partial^2 W_h}{\partial y^2} = \frac{\partial^2 W_h}{\partial r^2}(\frac{\partial r}{\partial y})^2 + \frac{\partial W_h}{\partial r}\frac{\partial^2 r}{\partial y^2} \tag{88}$$

$$\frac{\partial^2 W_h}{\partial x \partial y} = \frac{\partial^2 W_h}{\partial r^2}\frac{\partial r}{\partial x}\frac{\partial r}{\partial y} + \frac{\partial W_h}{\partial r}\frac{\partial^2 r}{\partial x \partial y} \tag{89}$$

$$\frac{\partial^2 W_h}{\partial x \partial h} = \frac{\partial^2 W_h}{\partial r \partial h}\frac{\partial r}{\partial x}\ , \quad \frac{\partial^2 W_h}{\partial y \partial h} = \frac{\partial^2 W_h}{\partial r \partial h}\frac{\partial r}{\partial y} \tag{90}$$

A.4 Equations of Motion in Polar Coordinates

Instead of Cartesian coordinates, as used in Eqs.(4) through) (6), it is also possible to use polar coordinates to describe the windshear terms in the equations of motion. In fact, this particular formulation has already been used to express the F-factor in Eq. (25).

This Section presents the equations of motion in terms of polar coordinates:

$$\dot{E} = \frac{(T - D)V}{W} + W_h - \frac{V\cos\gamma}{g}\{V\cos\gamma[\frac{\partial W_r}{\partial r}\cos^2(\chi - \chi_w) + \frac{W_r}{r}\sin^2(\chi - \chi_w)] + W_r\frac{\partial W_r}{\partial r}\cos(\chi - \chi_w)\} - \frac{V\sin\gamma}{g}\{\frac{\partial W_r}{\partial r}[W_r + V\cos\gamma\cos(\chi - \chi_w)] + \frac{\partial W_h}{\partial h}[W_h + V\sin\gamma]\} \tag{91}$$

$$\dot{\gamma} = \frac{g}{V}[\frac{L\cos\mu}{W} - \cos\gamma] + \frac{\sin\gamma}{V}\{V\cos\gamma[\frac{\partial W_r}{\partial r}\cos^2(\chi - \chi_w) + \frac{W_r}{r}\sin^2(\chi - \chi_w)] + W_r\frac{\partial W_r}{\partial r}\cos(\chi - \chi_w)\} - \frac{\cos\gamma}{V}\{\frac{\partial W_r}{\partial r}[W_r + V\cos\gamma\cos(\chi - \chi_w)] + \frac{\partial W_h}{\partial h}[W_h + V\sin\gamma]\} \tag{92}$$

$$\dot{\chi} = \frac{g}{V\cos\gamma}\frac{L\sin\mu}{W} + [\frac{\partial W_r}{\partial r} - \frac{W_r}{r}]\sin(\chi - \chi_w)\cos(\chi - \chi_w) + \frac{W_r}{V\cos\gamma}\frac{\partial W_r}{\partial r}\sin(\chi - \chi_w) \tag{93}$$